Characterization of Second and Third Order Susceptibilities in Organic Salts

by

Brian Lee Lawrence

Submitted to the Department of Electrical Engineering and Computer Science
in partial fulfillment of the requirements for the degrees of

Master of Science

and

Bachelor of Science in Electrical Engineering

at the

MASSACHUSETTS INSTITUTE OF TECHNOLOGY

May 1992

Author_____
Department of Electrical Engineering and Computer Science
May 8, 1992

Certified by_____
Dr. Christopher P. Yakymyshyn
Company Supervisor
Thesis Supervisor

Certified by_____
Erich P. Ippen
Professor of Electrical Engineering
Thesis Supervisor

Certified by_____
Dr. Kirby G. Vosburgh
Manager Applied Physics Laboratory
Thesis Supervisor

Accepted by_____
Campbell L. Searle
Chairman, Departmental Committee on Graduate Students

Characterization of Second and Third Order Susceptibilities in Organic Salts

by

Brian Lee Lawrence

Submitted to the Department of Electrical Engineering and Computer Science
on May 8, 1992, in partial fulfillment of the
requirements for the degrees of
Master of Science
and
Bachelor of Science in Electrical Engineering

Abstract

The field of nonlinear optics is currently, and unfortunately, restricted to high-power applications. Available materials do not yet have large enough nonlinear coefficients to reduce the large power requirements. However, new organic materials based on stilbene and stilbazole chromophores crystallized with a variety of counterions open new possibilities for low power observable nonlinear phenomena. The next significant step is to accurately characterize the second and third order susceptibilities of these materials. In this thesis, over 50 different organic compounds were evaluated. The powder forms of the materials were tested using a scattered harmonic intensity powder test for both second and third order nonlinearities at a fundamental wavelength of 1.907 μm. The most significant of the materials exhibited second harmonic efficiencies of roughly 1000 to 2500 times Urea. The best third order materials exhibited efficiencies approximately 50 to 200 times DimethylAmino NitroStilbene (DANS). Crystals of one of the materials, DimethylAmino Stilbazolium Tosylate (DAST), were grown and characterized using a second harmonic Maker Fringe measurement at 1.907 μm. The DAST crystals exhibited a d_{11} coefficient of 600$\pm$100 pm/V with a coherence length, L_c, of 2.6$\pm$0.3 μm. The measurements showed a d_{12} coefficient of 230$\pm$50 pm/V, L_c=1.7$\pm$0.2 μm. These results gave a FOM of approximately 4000 (pm/V)^2. An evaluation of the measurements relative to current materials and device requirements is presented.

Thesis Supervisor: Dr. Christopher P. Yakymyshyn
Title: Company Supervisor

Thesis Supervisor: Erich P. Ippen
Title: Professor of Electrical Engineering

Thesis Supervisor: Dr. Kirby G. Vosburgh
Title: Manager Applied Physics Laboratory

Acknowledgments

I would like to thank Dr. Chris Yakymyshyn, Dr. William Lotshaw, Dr. Kevin Stewart, Dr. Manny Aven, and Dr. Kirby Vosburgh as well as the General Electric Company for allowing me the opportunity to conduct this research at the General Electric Research and Development Center. In addition, I extend my gratitude to David Fobare, Dr. Doug Doughty, and Dr. Robert Black for their invaluable assistance and friendship during my stay in Schenectady.

I would like to thank Professor Erich Ippen for his assistance, supervision, and support, for which I am deeply indebted.

I would also like to thank Mom, Dad, Jeff, Jennie, Clyde, Katie, Bonnie, and Licorice, for their love and support in this endeavor, and for believing in me even when I had doubts.

This work represents the culmination of my studies at the Massachusetts Institute of Technology. Over the past five years, a great many people have passed in and out of my life as I traversed the many mazes that make up MIT. From the experiences, I carried away a wealth of wisdom, and from each person that has influenced my life in any way a little piece is included in this work. To all of those people, professors, acquaintances, teammates, brothers, coworkers and friends I owe a great deal. Thank you all.

Life at M.I.T.
The reward was worth the work
The light bulb turns on

Contents

List of Figures

List of Tables

Chapter 1

Introduction

Optics, the study of light, is a field that has been investigated for many centuries. However, the interaction of light and matter has only recently received attention. Not until the birth of quantum mechanics in the early and middle twentieth century, could a true understanding of light–matter interactions be developed. With a clearer picture of the nature of light and atoms, and with the basic principles of quantum mechanics substantiated, the field of nonlinear optics was born.

1.1 Nonlinear Optics

Initially, scientists believed that the propagation of light in a medium was a linear phenomena. As a beam propagates through a material, the electric field component of the beam induces a polarization. This polarization is due to electronic oscillations around the particular atoms that compose the material, and may be altered by ionic motion which perturbs the electron distribution. Typically, these oscillations are modeled as a simple mass–spring system. From this model, an expression for the induced polarization can be derived as in equation 1.1

$$\mathbf{P} = \mathbf{P}_o + \epsilon_o \chi \mathbf{E} \tag{1.1}$$

In equation 1.1, χ is the dielectric susceptibility, $\mathbf{E}$ is the electric field component of the propagating beam, and $\mathbf{P}_o$ is the characteristic polarization of the material. For most commonly encountered circumstances, the linear approximation to the polarization gave

reasonable results. More recent research has indicated that Maxwell's equations, and consequently the wave equation, are not entirely linear in a medium. Most materials can successfully be approximated as linear, as the coefficients for the higher order, or nonlinear, terms are extremely small. Under the proper conditions, however, these nonlinearities can yield observable phenomena. In such cases, the linear approximation breaks down, and the expression for the polarization must then be written as in equation 1.2.

$$\mathbf{P} = \mathbf{P}_o + \epsilon_o \chi^{(1)}\mathbf{E} + \epsilon_o \chi^{(2)}\mathbf{E}^2 + \epsilon_o \chi^{(3)}\mathbf{E}^3 + ...\epsilon_o \chi^{(n)}\mathbf{E}^n \tag{1.2}$$

The dielectric susceptibility has been expanded to include higher order terms. In many cases, the polarization is written in terms of nonlinear coefficients **d** and **C** which represent second and third order nonlinearities, respectively. The relationship of the nonlinear optical coefficients to their respective susceptibilities is governed by the expressions in 1.3 and 1.4.[28][4][33]

$$d_{ijk} = \frac{\chi^{(2)}_{ijk}}{2} \tag{1.3}$$

$$C_{ijkl} = \frac{\chi^{(3)}_{ijkl}}{4} \tag{1.4}$$

The **d** and **C** coefficients are tensor quantities and may be represented in matrix form when contracted notation is used. The simplified notation arises from the fact that j and k in equation 1.3 are interchangeable (similar simplifications apply to the third order coefficients, but will not be dealt with here). The implication is that $d_{ijk} = d_{ikj}$, known as Kleinman symmetry.[6] The simplification of the various indices is then given by 1.5.

$$\begin{aligned} xx &= 1 \\ yy &= 2 \\ zz &= 3 \\ yz = zy &= 4 \\ xz = zx &= 5 \\ xy = yx &= 6 \end{aligned} \tag{1.5}$$

The contracted indices result in a 3x6 matrix representation for **d** that operates on the $\mathbf{E}^2$ column tensor to produce the components of the second harmonic polarization. The matrix multiplication is given in equation 1.6.

$$\begin{pmatrix} P_x \\ P_y \\ P_z \end{pmatrix} = \begin{pmatrix} d_{11} & d_{12} & d_{13} & d_{14} & d_{15} & d_{16} \\ d_{21} & d_{22} & d_{23} & d_{24} & d_{25} & d_{25} \\ d_{31} & d_{32} & d_{33} & d_{34} & d_{35} & d_{36} \end{pmatrix} \begin{pmatrix} E_x^2 \\ E_y^2 \\ E_z^2 \\ 2E_zE_y \\ 2E_zE_x \\ 2E_xE_y \end{pmatrix} \tag{1.6}$$

Symmetry considerations in most materials may simplify the matrix. Many times, certain elements go to zero or have the same magnitude as other tensor components within the matrix, simplifying the polarization expressions significantly. Under certain conditions, all elements may simultaneously go to zero. Specifically, for any crystal structure that is centrosymmetric the d_{ijk} tensor vanishes. Centric crystals require that a reversal of the signs of the electric field components cause a reversal of the sign of the polarization. However, since the polarization goes as the square of the fields, sign reversal has no effect, as shown in 1.7. Therefore, centrosymmetric crystals have a vanishing **d** coefficient, $d_{ijk} \equiv 0$. Unlike second order nonlinearities, third order effects do not require acentric crystallization to obtain non–vanishing third order susceptibilities. [4]

$$-P_i = -d_{ijk}E_jE_k \neq d_{ijk}(-E_j)(-E_k) \tag{1.7}$$

As is common in power series expansions, higher order coefficients tend to drop off rapidly. The expanded susceptibilities are no different. Direct fourth order and higher order effects generally do not produce measurable phenomena in existing materials, except when large intensities are used at the absorption resonance frequencies of the material. For this reason, many of the useful applications of nonlinear optical effects rely on second and third order responses. The effects important to the work detailed in this paper are: frequency conversion, the Pockel's electro-optic effect, and the optical Kerr effect.

1.1.1 Frequency Conversion

One of the most common observable nonlinear optical phenomena is the generation of new frequencies from an incident wave. Typically, the conversion process is considered in the realm of sum and difference frequency generation. Consider an optical beam composed of two plane waves having frequencies ω_1 and ω_2, respectively, as given in equation 1.8.

$$\mathbf{E} = \frac{\mathbf{E_1}(\omega_1)(e^{i\omega_1 t} + e^{-i\omega_1 t}) + \mathbf{E_2}(\omega_2)(e^{i\omega_2 t} + e^{-i\omega_2 t})}{2} \tag{1.8}$$

If the given wave were incident on a nonlinear material, a polarization would be induced in the medium. This polarization is given in 1.2. The incident field in 1.8 may be substituted into the expression for the polarization to arrive at equation 1.9; the substitution for the nonlinear optical coefficients has been made. The expression for the total polarization contains dc terms, terms at the incident wave frequencies, and terms at the sum and difference frequencies.

$$\begin{aligned}\mathbf{P} = \mathbf{P}_o + \epsilon_o \chi^{(1)} &\left[\frac{\mathbf{E_1}(\omega_1)(e^{i\omega_1 t} + e^{-i\omega_1 t}) + \mathbf{E_2}(\omega_2)(e^{i\omega_2 t} + e^{-i\omega_2 t})}{2}\right] + \\ &2d_{ij}\left[\frac{\mathbf{E_1^2}(\omega_1) + \mathbf{E_2^2}(\omega_2)}{2} + \frac{\mathbf{E_1^2}(\omega_1)}{4}(e^{i2\omega_1 t} + e^{-i2\omega_1 t})\right. \\ &\qquad + \frac{\mathbf{E_2^2}(\omega_2)}{4}(e^{i2\omega_2 t} + e^{-i2\omega_2 t}) \\ &\qquad + \frac{\mathbf{E_1}(\omega_1)\mathbf{E_2}(\omega_2)}{2}(e^{i(\omega_1+\omega_2)t} + e^{-i(\omega_1+\omega_2)t}) \\ &\qquad \left. + \frac{\mathbf{E_1}(\omega_1)\mathbf{E_2}(\omega_2)}{2}(e^{i(\omega_1-\omega_2)t} + e^{-i(\omega_1-\omega_2)t})\right] \ldots\end{aligned} \tag{1.9}$$

The expression can be rewritten, grouping the induced polarizations by frequency. The result is given in 1.10.

$$\mathbf{P} = \mathbf{P}_o + \mathbf{P}_{dc} + \mathbf{P}_{\omega_1,\omega_2} + \mathbf{P}_{2\omega_1} + \mathbf{P}_{2\omega_2} + \mathbf{P}_{\omega_1+\omega_2} + \mathbf{P}_{\omega_1-\omega_2} \tag{1.10}$$

The interesting terms in the polarization are those pertaining to the newly created frequencies at the second harmonic and at the sum and difference frequencies given in 1.11, 1.12, and 1.13.

$$\mathbf{P}_{2\omega} = \mathbf{P}_{2\omega_1} + \mathbf{P}_{2\omega_2} = \frac{d_{ij}}{2}\left[\mathbf{E}_1^2(\omega_1)(e^{i2\omega_1 t} + e^{-i2\omega_1 t}) + \mathbf{E}_2^2(\omega_2)(e^{i2\omega_2 t} + e^{-i2\omega_2 t})\right] \quad (1.11)$$

$$\mathbf{P}_{\omega_1-\omega_2} = d_{ij}\left[\mathbf{E}_1(\omega_1)\mathbf{E}_2(\omega_2)(e^{i(\omega_1-\omega_2)t} + e^{-i(\omega_1-\omega_2)t})\right] \quad (1.12)$$

$$\mathbf{P}_{\omega_1+\omega_2} = d_{ij}\left[\mathbf{E}_1(\omega_1)\mathbf{E}_2(\omega_2)(e^{i(\omega_1+\omega_2)t} + e^{-i(\omega_1+\omega_2)t})\right] \quad (1.13)$$

Therefore, given a material with a nontrivial **d** coefficient, and an incident field composed of two separate, unequal frequencies, the resultant output will have components at the second harmonic frequencies, and at the sum and difference frequencies. For a significant second order nonlinear coefficient, the harmonic, sum, and difference frequencies will be at observable intensities. Similar equations hold for third order nonlinearities, and a sizable **C** coefficient.

Under certain conditions, the nonlinearity of the material can be greatly enhanced. Consider the wave indicated in 1.8 now with a single frequency, $\omega_1 = \omega_2 = \omega$. Under this condition, the terms in equation 1.9 condense to oscillations at the fundamental frequency, ω, and the second harmonic, 2ω. For a sizable d_{ij} component, a monochromatic incident beam will yield outputs at the fundamental and at the second harmonic (in reality, there will be output components at a variety of frequencies, all of which will be multiples of the fundamental created by cascaded frequency summations).

To account for observable harmonic generation, the macroscopic physical system must be accounted for. Typically, an incident beam generates second harmonic fields throughout the bulk. The second harmonic generated at one point and having propagated to a second, will constructively or destructively interfere with the second harmonic wave generated at the new location. Ultimately, the phase–mismatch can be given by the difference in the propagation vector of the fundamental and harmonic beams, as shown in 1.14.

$$\Delta k = 2k_\omega - k_{2\omega} \quad (1.14)$$

For a nonzero phase–mismatch, the second harmonic generated at one point and that at another point yield a spatial interference pattern within the material. The total second harmonic power will be proportional to this interference pattern and may be given by the $sinc^2(x)$ function shown in 1.15.

$$P_{2\omega} \propto \frac{\sin^2(\frac{\Delta kL}{2})}{\left(\frac{\Delta kL}{2}\right)^2} \tag{1.15}$$

The distance within the material over which the two waves completely constructively or destructively interfere is called the coherence length. This maximum interference occurs wherever the phase–mismatch is a multiple of π. The coherence length may then be given by equation 1.16.

$$L_c = \frac{\pi}{\Delta k} = \frac{\lambda}{4(n_{2\omega} - n_{\omega})} \tag{1.16}$$

The coherence length and the spatial interference pattern become useful tools in the measurement of nonlinearities in a material. As a crystal is rotated in a beam, the optical length within the material changes. Consequently, the spatial interference pattern adjusts with angle resulting in output fringes. From the fringes, a coherence length and a nonlinear optical coefficient can be determined for a given material.

1.1.2 Linear Electro-optic Effect

The most widely used nonlinear phenomena is the linear electro–optic effect, also known as the Pockel's effect. In any system where the material characteristics can be effected by a field, the response is considered nonlinear. In the case of frequency conversion, the nonlinearities arise due to the electric field component of the incident optical wave. However, material changes can also occur due to an externally applied electric field and still yield nonlinear results. In this case, the phase or amplitude characteristics of a propagating wave can be altered, as opposed to the frequency.

The linear electro–optic effect is expressed in terms of a tensor quantity, $\mathbf{r}$. The various components of the electro–optics tensor, also called the Pockel's coefficient, can be simplified using a contracted notation similar to that used for the $\mathbf{d}$ coefficient. The simplification results in a 6x3 matrix as shown in 1.17.

$$\begin{pmatrix} r_{11} & r_{12} & r_{13} \\ r_{21} & r_{22} & r_{23} \\ r_{31} & r_{32} & r_{33} \\ r_{41} & r_{42} & r_{43} \\ r_{51} & r_{52} & r_{53} \\ r_{61} & r_{62} & r_{63} \end{pmatrix} \tag{1.17}$$

The resultant tensor represented by the matrix operates on the E column tensor to yield the changes in refractive index due to an applied field. In almost all cases, symmetry considerations cause the matrix to reduce to a markedly simplified form. In addition, assuming an appled field in a single direction the overall multiplication reduces greatly. Consider, as an example, the linear electro–optic effect in potassium dihydrogen phosphate (KDP), which crystallizes in a tetragonal space group, point group $\bar{4}2m$.[33] The only nonzero elements of the tensor are $r_{41} = r_{52}$ and r_{63}. To simplify things further, suppose the applied electric field is solely in the z direction. The resulting index ellipsoid may be given as in equation 1.18.

$$\frac{x^2 + y^2}{n_o^2} + \frac{z^2}{n_e^2} + 2r_{63}E_z xy = 1 \tag{1.18}$$

To find the resulting change in n due to the applied field, the expression in 1.18 must be rearranged. A coordinate transformation may be performed to obtain the resulting equation given in 1.19.

$$\frac{x'^2}{n_{x'}^2} + \frac{y'^2}{n_{y'}^2} + \frac{z'^2}{n_{z'}^2} = 1 \tag{1.19}$$

The z axis remains unchanged due to the absence of terms in 1.18 that effect the z component. On the other hand the components of x and y experience an identical change. The symmetry of 1.18 results in a coordinate transformation of 45°. The resulting index ellipsoid is given in 1.20.

$$\left(\frac{1}{n_o^2} + r_{63}E_z\right)x'^2 + \left(\frac{1}{n_o^2} - r_{63}E_z\right)y'^2 + \frac{z^2}{n_e^2} = 1 \tag{1.20}$$

Typically, $r_{63}E_z$ is significantly less than $\frac{1}{n_o^2}$ and can be treated as a small change, Δn. By using the differential relation given in 1.21, the indices of refraction on the transformed

axes, x' and y', can be derived. The three indices are given in 1.22.

$$dx = -\frac{1}{2}x^3 d\left(\frac{1}{x^2}\right) \tag{1.21}$$

$$\begin{aligned} n_{x'} &= n_o - \frac{1}{2}n_o^3 r_{63} E_z \\ n_{y'} &= n_o + \frac{1}{2}n_o^3 r_{63} E_z \\ n_{z'} &= n_e \end{aligned} \tag{1.22}$$

The electro–optic effect is a second order nonlinear phenomena, where an applied field induces changes in the material characteristics. The effect is similar to the changes induced in a material by a sufficiently intense optical field. In fact, the Pockel's coefficient can be related to the d coefficient through the relation given in 1.23, where ionic contributions have not been accounted for.[33]

$$r_{ijk} = -\frac{4\epsilon_o}{\epsilon_{ii}\epsilon_{jj}} d_{ijk} \tag{1.23}$$

1.1.3 Optical Kerr Effect

Second order nonlinear phenomena involve changes in a medium induced by an applied electric field. However, the nonlinear polarization expression, equation 1.2, is a Taylor series expansion and includes higher–order terms as well. While many of the higher–order terms may be neglected, The third order terms have the potential to induce changes in the material proportional to the square of an applied electric field. In the electro–optic realm, this is considered the quadratic electro–optic effect and is usually neglected in the presence of a linear phenomenon (although Kerr cells are useful in certain instances).

The square of an electric field is also proportional to an incident intensity. Thus third order effects may result in material changes due to the intensity of an incident optical beam. The effect is typically characterized as a refractive index change as shown in equation 1.24.[1]

$$n = n_o + \mathcal{J}|\mathbf{E}|^2 \tag{1.24}$$

In the expression for n, n_o is the linear refractive index, $\mathcal{J}$ is the optical Kerr coefficient,

and **E** is the electric field component of the optical beam. Often, the Kerr effect is expressed in terms of a nonlinear refractive index, n_2, as shown in 1.25.[12]

$$n = n_o + n_2 I = n_o + \Delta n_o \tag{1.25}$$

The result of an intensity dependent refractive index change is a phenomena known as self–focusing. A beam incident on a nonlinear material will experience refractive index changes across the wave front due to local intensity variations, and the wave front will begin to converge or diverge (depending on the sign of n_2). Ultimately, the beam undergoes a self–induced lensing effect within the material.

The self–focusing, or self–defocusing, phenomenon is the basis for a number of nonlinear measurement techniques. Using a focussed incident beam, and carefully analyzing the output, one can measure the nonlinear refractive index. From n_2, the third order nonlinear coefficient can be determined; such measurements serve as the basis for z-scan and pump–probe tests.

1.2 Applied Nonlinear Optics

Nonlinear optical materials produce interesting phenomena. However, the attraction of improved materials goes well beyond purely scientific interest. In many physical systems, the effects of a nonlinear medium may produce useful devices. The realizable applications of optical nonlinearities are sparse because of the power constraints. For the majority of materials, the second and third order coefficients are too low, requiring very high powers in either incident optical beams or externally applied fields, to produce usable output.

The most commonly used nonlinear phenomenon is the linear electro–optic effect. The devices that utilize the Pockel's effect are electro–optic modulators, of which there are numerous examples. For amplitude and phase modulation of a propagating beam, low frequency applied fields can be used in longitudinal or transverse device structures. For modulation at high frequencies and large bandwidths, traveling wave modulators are typically used. In addition, electro–optic modulators may also be used to deflect incident beams of light. The currently available materials provide good modulating capability at low frequencies. However, optical signals carry information at higher bandwidths and with lower loss and power dissipation than electrical signals in metallic conductors. To create a high

bandwidth modulator, materials with low dielectric constants are necessary, to provide a reduction in the velocity mismatch between RF and optical waves.[18] Furthermore, for commercial uses the stability and damage thresholds must be improved over existing materials. Finally, increased linear electro-optic coefficients allow lower voltages to be applied to obtain the same results, reducing overall power requirements.

Efficient frequency doubling has also recently become a highly investigated phenomenon. Frequency doublers for high-power lasers have been the primary use of nonlinear phenomena at optical frequencies. However, over the past few years, applications of efficient frequency doubling at low powers have become important. Notably, applications have arisen in data storage and duplicating techniques utilizing gallium arsenide (GaAs) lasers operating in the 100 mW range.[23] Therefore, to obtain useful and efficient conversion to the doubled frequency at such relatively low powers, materials with significantly higher second order nonlinear coefficients than those currently available are necessary. Furthermore, the materials must be processable to create integrated devices for these new applications.

Third order nonlinear phenomena have also become significant. New device possibilities have been suggested in signal processing, amplification, beam steering, and image processing.[4] The most promising potential use of third order materials is in "all-optical" computing, where two third-order nonlinear processes become important. First, integrated device technology for beam steering to send the beam where necessary would be required. Second, optical spatial light modulation would play a major role in fully optical devices.[4] Such modulators are typically electro-optic devices; however, all-optical modulators may become real devices with good quality third order nonlinear materials.

1.3 Nonlinear Optical Materials

The applications of nonlinear optics have been limited by the lack of suitable materials. Nonlinear optical materials have been available for frequency conversion and other limited applications. However, currently available materials require powers of 100 W to 10 kW to obtain observable nonlinear optical phenomena.[25] Therefore, by producing new materials with higher nonlinear coefficients, the powers necessary to produce useful effects may be reduced. The work done in this paper advocates the use of organic materials over traditional inorganics to achieve improved performance.

Nonlinear optical effects are due to a polarization created by intense electric or electromagnetic fields. The polarization has already been discussed for bulk materials (see section 1.1). However, the source of the bulk effects is found at a molecular level. The polarization is given by the field-dependent induced dipole moment shown in 1.26.

$$\mu = \mu_o + \alpha \mathbf{E} + \beta \mathbf{E}^2 + \gamma \mathbf{E}^3 + \cdots \tag{1.26}$$

In equation 1.26, μ_o is the natural dipole moment, α is the polarizability, β is the hyperpolarizability, and γ is the second hyperpolarizability of the molecule.[4] The polarizability constants of the material describe the molecular response to perturbation by electric fields or electromagnetic radiation, and thus give rise to the source of nonlinearities at a molecular level.

1.3.1 Inorganic Compounds

Traditionally, nonlinear materials have been inorganic. Such notable crystals as the previously discussed KDP, lithium niobate, and potassium titanyl phosphate (KTP) have been widely used for frequency doubling in high power lasers or electro-optic modulation. Unfortunately, the applications are limited due to the relatively low nonlinear response of even the best phase matched materials. The lack of significant nonlinearities comes from the atomic or molecular mechanism responsible for the phenomena.

Inorganic compounds typically form ionic bond structures. Many of the molecules have a significant hyperpolarizability, β, and therefore have a large second order dipole response. At the molecular level, a large second order response indicates that the electron cloud surrounding the ion experiences substantial oscillations when driven by a sufficiently intense field. The nonlinear effect arises from dipolar contributions of an ion and all of its neighbors.

Induced polarization in the inorganic family of nonlinear materials is a result of electronic motion about the atoms in the lattice structure of the crystal. As the electron cloud surrounding a particular ion in the crystal oscillates, electrostatic interactions with neighboring ions cause distortions, which give rise to the nonlinear optical phenomena. The distortions of the electron cloud motion are due to lattice vibrations, or phonon contributions, that alter the separation of the ions increasing or decreasing the Coulombic potential and adjusting the force acting on the electron cloud.[18] Inherently, because ionic motion is

much slower than electronic motion, ionic contributions enhance Pockel's and dc Kerr effects (low frequency effects), but do not contribute to nonlinear effects involving solely fields at optical frequencies. In addition, the ionic contribution usually implies a large low-frequency dielectric constant, an undesirable property when considering device architecture.[31]

1.3.2 Organic Compounds

The use of organic media as a means of producing nonlinear optical phenomena is a recent discovery. However, there have already been significant advances resulting in such materials as 2-methyl-4-nitroaniline (MNA) and 4-dimethylamino-nitrostilbene (DANS). These materials rival the most widely used inorganic nonlinear media, but the crystallization process is not yet widely understood and therefore, the organics have not yet made a dent into the scientific and commercial uses of nonlinear optical materials.

Organic materials offer the possibility of rivaling or even besting inorganic materials in nonlinear response. There are additional advantages to these substances as well. Organic materials can be engineered with a high degree of accuracy to produce enhanced characteristics. The nature of organic molecules implies that electronic, not ionic, motion will generate optical responses. Inherently, electronic responses are faster than ionic and result in greatly increased response times.[18] In addition, these materials offer the potential for large, broadband electro-optic coefficients while maintaining relatively small low-frequency dielectric constants.[18] Additionally, the damage thresholds are at least comparable to those of inorganic materials.[28] Ultimately, organic materials may be more readily usable for devices where their inorganic counterparts proved insufficient.

As with inorganic materials, many of the organic molecules have significant hyperpolarizabilities.[21] The bond structures, on the other hand, are typically covalent. The dipole moment arises from oscillations of electrons along the length of the molecule. The dipolar oscillations can be enhanced through careful engineering of the molecular structure. The length of the molecule corresponds directly to the length of electric dipole induced in the material. The increased dipole length subsequently results in a larger dipole moment. Furthermore, an alternating bond structure facilitates electron motion along the molecular length. The conjugated structure is one in which the bonds alternate: single-double, double-triple, single-triple or some combination thereof. Finally, a properly substituted system is also known to enhance molecular nonlinear response, where electron donors and

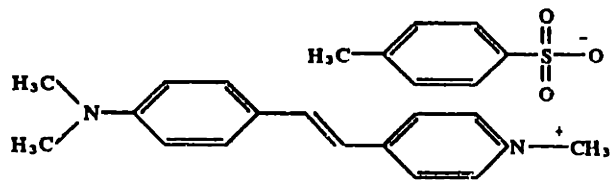

Figure 1-1: DimethylAmino Stilbazolium Tosylate

acceptors are carefully placed to create a large electric dipole moment.[16] The molecular systems studied here were based on a strategically designed system, an example of which, dimethylamino stilbazolium tosylate (DAST), is given in figure 1-1.

The magnitudes of the macroscopic nonlinearities depend critically on the molecular packing arrangement. Third order effects are observed in nearly all phases of matter, but can be significantly enhanced through proper molecular orientation.[13] However, second harmonic generation requires that the molecules exist in a noncentrosymmetric environment to obtain sizable bulk effect.[15] Unfortunately, large electron-donating and electron-withdrawing substituents invariably result in large molecular dipoles, whose neutral dipolar interactions tend to drive the crystallization into a centric structure. It has been suggested that strong coulombic interactions may override dipolar ones and result in acentric crystal structures. In fact, this approach was extended to a series of organic salts in which a cationic chromophore with a large molecular hyperpolarizability, β, was crystallized with a variety of counterions.[2][21][7]

The work discussed in this paper concentrates on the measurements of the second and third order optical nonlinearities in some of the recently uncovered organic salts.[21][2] The family of salts investigated is based on the stilbene and stilbazole chromophores combined with a number of counterions including the tosylate and mesylate ions. Chapter two describes the theory underlying the techniques used for the measurement of nonlinear coefficients. Chapter three gives the experimental setup and procedures used to perform the tests. Chapter four gives the results of the experiments and an analysis of these results to obtain values for the coefficients. Chapter five contains concluding remarks regarding the relative potential of these tests and materials for future use.

Chapter 2

Nonlinear Optical Characterization

As discussed in chapter 1, optical nonlinearities are a result of a polarization induced in a medium. The expression for the induced polarization, equation 1.2, can be rewritten to form an expression in terms of an effective dielectric susceptibility. The result is given in equation 2.1.

$$\mathbf{P} = \mathbf{P}_o + \epsilon_o[\chi^{(1)} + \chi^{(2)}\mathbf{E} + \chi^{(3)}\mathbf{E}^2 + ...\chi^{(n)}\mathbf{E}^{n-1}]\mathbf{E} \tag{2.1}$$

The effective dielectric susceptibility is now represented as an expansion with higher order terms that are dependent on increasing powers of the incident electric field. The field dependence of the nonlinear terms in χ is the key to measuring the second and third order susceptibilities, $\chi^{(2)}$ and $\chi^{(3)}$, respectively. By using an incident beam to generate nonlinearities within the sample material, a careful analysis of the output can lead to measurements of the coefficients (fourth order and higher order terms do not produce measurable output except under extremely rare conditions). This method, the use of the field dependence, is the most widely used measurement method forming the basis for many techniques: Powder tests, Maker Fringe tests, Z-scan measurements, and Pump–probe tests.

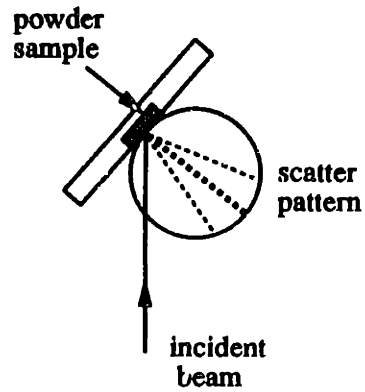

Figure 2-1: Scatter pattern for reflection measurement

2.1 The Powder Test

The powder technique was initially detailed in the work of Kurtz and Perry [8]. This method is a qualitative test that allows for a general classification of the magnitude of the second or third order optical nonlinearity in a given material. The classification is relative to a reference substance that has already been well characterized, in this work, Urea. The test is relatively simple to conduct and involves illuminating a powdered sample with a laser and ob rving the second or third harmonic intensity generated.

The original test, as proposed by Kurtz and Perry, used a transmission technique whereby the sample was illuminated at normal incidence and the transmitted intensity was measured. However, in this work a reflection technique is proposed in which the sample is illuminated at an oblique incident angle and the reflected second or third harmonic intensity is measured. The powder material is not placed in index matching fluid and thus the scatter pattern of the reflected power is nearly Lambertian [8] as shown in figure 2-1.

Additionally, the various compounds and their differing phases are unsized; but typical particle dimensions are on the order of 50 to 150 μm. The sample container is constructed to accommodate a sample layer approximately 400 to 500 μm thick. The diameter of the incident beam is approximately 5 mm. The experiment is conducted in the region where particle size is significantly smaller than the sample layer thickness which is, in turn, significantly smaller than the incident beam diameter. Operating in this region insures that the incident beam strikes a large number of particles with random orientations, thus providing a statistical average. Furthermore, the particle sizes are assumed to be significantly larger than the coherence length of the material, avoiding any correlations between the second or

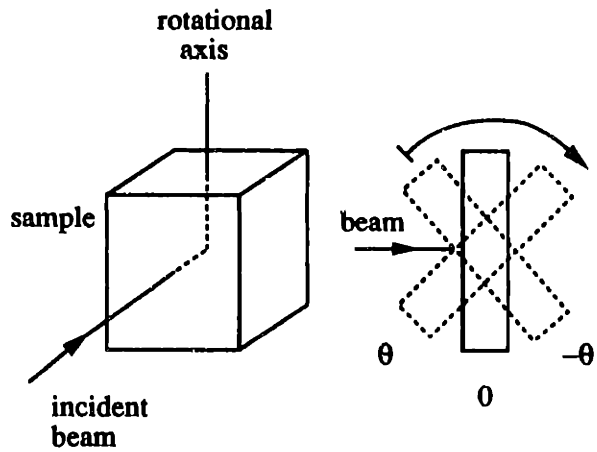

Figure 2-2: Maker Fringe measurement rotation

third harmonic intensities generated by individual particles.

The fundamental wavelength for the powder tests is 1.907 μm. This wavelength is chosen because some of the stilbazole and stilbene based organic salts have large absorption resonances in the visible region of the spectrum. However, these same materials are nearly transparent at 1.907 μm and at the second harmonic wavelength of 953.5 nm. In addition, many of the compounds are also transparent at the third harmonic wavelength of 635.7 nm. Both the second and third harmonic tests are conducted in identical fashion using different filters where appropriate.

2.2 The Maker Fringe Test

Unlike the powder test detailed in the previous section, the Maker Fringe test is a quantitative test that will yield numerical results for the second and third order nonlinear coefficients, d_{ij} and C_{ij}, respectively. However, the tests are similar in that both provide results relative to a reference material. The reference material used for the Maker Fringe tests is a single crystal of lithium niobate, $LiNbO_3$. This technique was first suggested in the work of Maker and others [17], and expanded upon by Kurtz and Jerphagnon [5]. To obtain measurements of the nonlinear coefficients, a single crystal of a material is placed at the focus of a beam and rotated from a positive angular inclination to the beam, through normal, to a negative angular inclination, as shown in figure 2-2. As the crystal is rotated, the second or third harmonic output is measured.

2.2.1 Second Harmonic Measurements

Under ideal circumstances, the second harmonic generated within a bulk nonlinear crystal is proportional to a $sinc^2(x)$ function, where x includes terms to account for the variation in optical path length in the material due to angular rotation. The full expression for the second harmonic power may be given by equation 2.2 [28].

$$P_{2\omega} = \left[\frac{L^2\omega^2}{2\epsilon_o c^3 A}\right] \frac{1}{n_\omega^2 n_{2\omega}} d_{ij}^2 P_\omega^2 sinc^2\left(\frac{\Delta k}{2}L\right) \tag{2.2}$$

In this expression, L is the crystal thickness at normal incidence, ω is the frequency of the fundamental beam, A is the "spot size" of the beam (for our purposes the spot size is πw_o^2, where w_o is the beam waist at the focus for a gaussian beam), d_{ij} is the second-order nonlinear coefficient, P_ω is the incident fundamental power, and Δk is the phase mismatch ($\Delta k = 2k_\omega - k_{2\omega}$). The expression given in 2.2 is valid only when the sample is considered thin. Under this assumption, L is less than the confocal parameter, $\frac{\pi w_o^2}{\lambda}$. Therefore, changes in the beam diameter within the crystal due to diffraction or refraction can be neglected.

The Maker Fringe curves are based on transmitted second harmonic power, and thus involve some additional complexity. To account for fresnel losses as the beam passes into and out of the crystal, two transmission factors are included. The first, $T_\omega(\theta)$, incorporates the fresnel losses at the front surface in the fundamental beam, that is, at frequency ω. The second, $T_{2\omega}(\theta)$, accounts for fresnel losses at the back surface in the second harmonic output, at frequency 2ω. Additional correction factors need to be included to take into account the various causes of departure from the ideal case. These additional terms include corrections for multiple reflections, $R(\theta)$, a beam size correction, $B(\theta)$, and the angular dependence of the d_{ij} coefficient, $p(\theta)$, where θ is the angle of incidence. Including these terms results in the most general expression for the second harmonic power generated in, and transmitted through, a nonlinear crystal, as given in equation 2.3.

$$P_{2\omega} = \left[\frac{L^2\omega^2}{2\epsilon_o c^3 A}\right] \frac{1}{n_\omega^2 n_{2\omega}} d_{ij}^2 P_\omega^2 T_\omega(\theta) T_{2\omega}(\theta) R(\theta) B(\theta) p(\theta) sinc^2\left(\frac{\Delta k}{2}L\right) \tag{2.3}$$

This expression may be simplified for the materials and circumstances specific to the work discussed in this paper. For materials with low refractive indices, the multiple reflection factor, R, is close to unity, and independent of θ [5]. In addition, when operating in the region where the crystal thickness, L, is less than the confocal distance, no beam

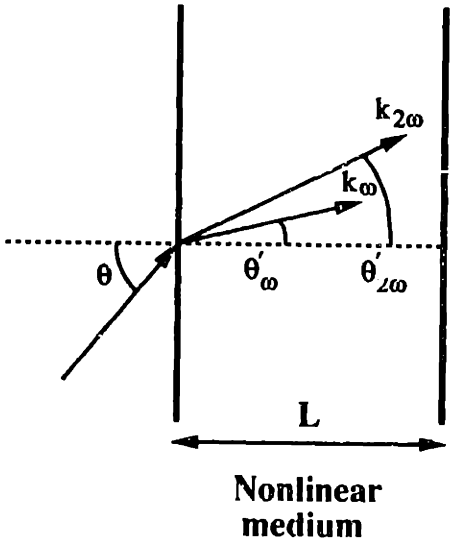

Figure 2-3: Internal angles

correction factor, B, is necessary [5]. Finally, by carefully choosing the orientation of the crystallographic axis, rotation axis, and fundamental electric field polarization, and by incorporating angular rotation into changes in optical path length, the angular dependence of d_{ij} can be eliminated, forcing p equal to unity. This leaves simply the transmission factors.

The transmission factors, $T_\omega(\theta)$ and $T_{2\omega}(\theta)$, are obtained from the solution of Maxwell's equations for transverse electric fields (those used in this work) with the appropriate boundary conditions, and are given in equations 2.4 and 2.5.

$$T_\omega(\theta) = \frac{2\cos\theta}{n_\omega \cos\theta'_\omega + \cos\theta} \tag{2.4}$$

$$T_{2\omega}(\theta) = \frac{2n_{2\omega}\cos\theta'_{2\omega}(\cos\theta + n_\omega\cos\theta'_\omega)(n_\omega\cos\theta'_\omega + n_{2\omega}\cos\theta'_{2\omega})}{(n_{2\omega}\cos\theta'_{2\omega} + \cos\theta)^3} \tag{2.5}$$

In these formulas, θ'_ω and $\theta'_{2\omega}$ are the internal angles for the fundamental and second harmonic beams, respectively. These internal angles are shown in figure 2-3.

The internal angles can be converted to functions of the original angle of incidence, θ, through the application of Snell's law.

$$\theta'_\omega = \arcsin\left(\frac{\sin\theta}{n_\omega}\right)$$

$$\theta'_{2\omega} = \arcsin\left(\frac{\sin\theta}{n_{2\omega}}\right)$$

Application of Snell's law to internal angles in the equations for the transmission coefficients, $T_\omega(\theta)$ and $T_{2\omega}(\theta)$, results in expressions dependent solely on the angle of incidence. The single variable transmission factors are then given by equations 2.6 and 2.7.

$$T_\omega(\theta) = \frac{2\cos\theta}{n_\omega \cos\left[\arcsin\left(\frac{\sin\theta}{n_\omega}\right)\right] + \cos\theta} \tag{2.6}$$

$$\begin{aligned} T_{2\omega}(\theta) = {} & \frac{2n_{2\omega}\cos\left[\arcsin\left(\frac{\sin\theta}{n_{2\omega}}\right)\right]}{\left(n_{2\omega}\cos\left[\arcsin\left(\frac{\sin\theta}{n_{2\omega}}\right)\right] + \cos\theta\right)^3} \times \\ & \left(\cos\theta + n_\omega \cos\left[\arcsin\left(\frac{\sin\theta}{n_\omega}\right)\right]\right) \times \\ & \left(n_\omega \cos\left[\arcsin\left(\frac{\sin\theta}{n_\omega}\right)\right] + n_{2\omega}\cos\left[\arcsin\left(\frac{\sin\theta}{n_{2\omega}}\right)\right]\right) \end{aligned} \tag{2.7}$$

The next step is to simplify the $sinc(x)$ function in the expression for the second harmonic power. By factoring out the denominator and expressing the phase mismatch, Δk, in terms of ω and the indices of refraction, the expression for the total second harmonic power transmitted by the crystal may be given be equation 2.8.

$$P_{2\omega} = \left[\frac{1}{2\epsilon_o c\pi w_o^2}\right] \frac{1}{n_\omega^2 n_{2\omega}(n_\omega - n_{2\omega})^2} d_{ij}^2 P_\omega^2 T_\omega(\theta) T_{2\omega}(\theta) \sin^2\left(\frac{\Delta k}{2}L\right) \tag{2.8}$$

The argument of the *sin* function may be simplified using appropriate assumptions about the coherence length and the optical path length in the crystal. The coherence length of a material is defined as the distance in the medium over which the power generated at different points completely constructively or destructively interferes. For example, the second harmonic signal generated at one point and having propagated a coherence length within the medium will be exactly out of phase with any second harmonic signal generated at the second location. Similarly, a distance of two coherence lengths would result in the signals being completely in phase. This implies that the coherence length is a result of a phase mismatch of π as shown in equation 2.9.

$$\Delta k L_c = \pi \tag{2.9}$$

Realistically, the coherence length is an angle-dependent quantity. However, a good

approximation is to assume that it is reasonably constant and instead incorporate the angular dependence into the optical path within the crystal. Thus, the coherence length may be defined as in equation 2.10.

$$L_c \approx L_c(0) = \frac{\pi}{\Delta k} = \frac{\lambda}{4(n_{2\omega} - n_\omega)} \tag{2.10}$$

Incorporating the angular dependence into the optical path length and substituting for the internal angles results in a new crystal thickness $L'(\theta)$ as given in 2.11.

$$L'(\theta) = \frac{L}{\cos\theta'_\omega} = \frac{L}{\cos\left[\arcsin\left(\frac{\sin\theta}{n_\omega}\right)\right]} \tag{2.11}$$

The coherence length and angular-dependent optical path length may now be used to simplify the argument of the *sin* function as shown in 2.12.

$$\frac{\Delta k(\theta)}{2}L = \frac{\pi}{2}\frac{\Delta k}{\pi}L'(\theta) = \frac{\pi}{2}\frac{L}{L_c(0)}\frac{1}{\cos\left[\arcsin\left(\frac{\sin\theta}{n_\omega}\right)\right]} \tag{2.12}$$

Using the angle dependent expressions for the transmission coefficients and the simplifications of the arguments to the *sin* function, an expression for the total transmitted second harmonic power as a function of the indices of refraction, the crystal thickness, the coherence length (at normal incidence), and the angle of incidence can be derived. Given that L, $L_c(0)$, n_ω, and $n_{2\omega}$ are material constants, the expression for the transmitted second harmonic power is dependent solely on the angle of incidence, θ, as given in 2.13.

$$P_{2\omega}(\theta) = \left[\frac{1}{2\epsilon_o c\pi w_o^2}\right]\frac{1}{n_\omega^2 n_{2\omega}(n_\omega - n_{2\omega})^2} d_{ij}^2 P_\omega^2 T_\omega(\theta) T_{2\omega}(\theta)\sin^2(\psi(\theta)) \tag{2.13}$$

where

$$\psi(\theta) = \frac{\pi}{2}\frac{L}{L_c(0)}\frac{1}{\cos\left[\arcsin\left(\frac{\sin\theta}{n_\omega}\right)\right]} \tag{2.14}$$

$$T_\omega(\theta) = \frac{2\cos\theta}{n_\omega\cos\left[\arcsin\left(\frac{\sin\theta}{n_\omega}\right)\right] + \cos\theta} \tag{2.15}$$

$$T_{2\omega}(\theta) = \frac{2n_{2\omega}\cos\left[\arcsin\left(\frac{\sin\theta}{n_{2\omega}}\right)\right]}{\left(n_{2\omega}\cos\left[\arcsin\left(\frac{\sin\theta}{n_{2\omega}}\right)\right] + \cos\theta\right)^3} \times$$

$$\left(\cos\theta + n_\omega \cos\left[\arcsin\left(\frac{\sin\theta}{n_\omega}\right)\right]\right) \times$$
$$\left(n_\omega \cos\left[\arcsin\left(\frac{\sin\theta}{n_\omega}\right)\right] + n_{2\omega} \cos\left[\arcsin\left(\frac{\sin\theta}{n_{2\omega}}\right)\right]\right) \tag{2.16}$$

The expression for the total transmitted second harmonic power predicts the shape of the curve for a specified thickness of a given material. The equations simplify remarkably when used, in conjunction with a reference material, to compute an element of the d coefficient tensor. Using the Maker Fringe experimental results to calculate a d_{ij} coefficient is a two step process. First a coherence length is calculated from the minima of the measured data. Second, using a reference material and the peak of the envelope curve of the fringes, a d_{ij} coefficient can be computed.

The first step, calculating the coherence length, does not require a reference material. These calculations are based on the locations of the minima of the fringes for the particular material. Returning to equation 2.13, the oscillations, or fringes, are a result of the $sin^2(\psi)$ portion of the expression. The zeros, or minima, occur where $sin(\psi)$ goes to zero as shown in 2.17, where the internal angle substitution has again been made.

$$\sin(\psi) = \sin\left(\frac{\pi}{2}\frac{L}{L_c(0)}\frac{1}{\cos\left[\arcsin\left(\frac{\sin\theta}{n_\omega}\right)\right]}\right) = 0 \tag{2.17}$$

This is true for the condition given in 2.18, where m is an integer.

$$\frac{\pi}{2}\frac{L}{L_c(0)}\frac{1}{\cos\left[\arcsin\left(\frac{\sin\theta}{n_\omega}\right)\right]} = m\pi \tag{2.18}$$

While the value of m is unknown, two adjacent minima can be given by m and $m+1$. This assumption yields two expressions for the m^{th} and $m^{th}+1$ minima as given in 2.19 and 2.20, where θ_m and θ_{m+1} are the incidence angles that give the m^{th} and $m^{th}+1$ minima.

$$m\pi = \frac{\pi}{2}\frac{L}{L_c(0)}\frac{1}{\cos\left[\arcsin\left(\frac{\sin\theta_m}{n_\omega}\right)\right]} \tag{2.19}$$

$$(m+1)\pi = \frac{\pi}{2}\frac{L}{L_c(0)}\frac{1}{\cos\left[\arcsin\left(\frac{\sin\theta_{m+1}}{n_\omega}\right)\right]} \tag{2.20}$$

Subtracting these two expressions yields 2.21.

$$\pi = \frac{\pi}{2}\frac{L}{L_c(0)}\left(\frac{1}{\cos\left[\arcsin\left(\frac{\sin\theta_{m+1}}{n_\omega}\right)\right]} - \frac{1}{\cos\left[\arcsin\left(\frac{\sin\theta_m}{n_\omega}\right)\right]}\right) \tag{2.21}$$

Algebraic simplification finally results in an expression from which the coherence length of the material may be calculated based on the minima alone, as given in equation 2.22

$$L_c(0) = \frac{L}{2}\left(\frac{1}{\cos\left[\arcsin\left(\frac{\sin\theta_{m+1}}{n_\omega}\right)\right]} - \frac{1}{\cos\left[\arcsin\left(\frac{\sin\theta_m}{n_\omega}\right)\right]}\right) \tag{2.22}$$

The second portion of the d_{ij} coefficient calculation requires some reworking of the expression for the second harmonic power. The peak power, or peak of the envelope curve, is the significant quantity; thus the $sin(\psi)$ term in equation 2.8 goes to unity. This assumption and some algebraic simplification yields expression 2.23.

$$P_{2\omega} = \left[\frac{2\omega^2}{\epsilon_o c^3 \pi w_o^2 \Delta k^2}\right]\frac{1}{n_\omega^2 n_{2\omega}} d_{ij}^2 P_\omega^2 T_\omega(\theta) T_{2\omega}(\theta) \tag{2.23}$$

Substitution of the expression for the coherence length, $L_c(0) = \frac{\pi}{\Delta k}$, results in expression 2.24.

$$P_{2\omega} = \left[\frac{2\omega^2}{\epsilon_o c^3 \pi^3 w_o^2}\right]\frac{1}{n_\omega^2 n_{2\omega}} L_c^2(0) d_{ij}^2 P_\omega^2 T_\omega(\theta) T_{2\omega}(\theta) \tag{2.24}$$

To compute the d_{ij} coefficient, the expression for the second harmonic power of the sample is divided by that of a known reference material. The peak of the envelope occurs at normal incidence, the two transmission factors are assumed to be similar in magnitude at normal incidence for both the sample and reference materials, and will thus be neglected. Performing the division (the s subscript indicates sample, and r indicates reference) yields expression 2.25.

$$\frac{P_{2\omega_s}}{P_{2\omega_r}} = \frac{\left[\frac{2\omega^2}{\epsilon_o c^3 \pi^3 w_o^2}\right]\frac{1}{n_{\omega_s}^2 n_{2\omega_s}} L_{c_s}^2(0) d_s^2 P_\omega^2}{\left[\frac{2\omega^2}{\epsilon_o c^3 \pi^3 w_o^2}\right]\frac{1}{n_{\omega_r}^2 n_{2\omega_r}} L_{c_r}^2(0) d_r^2 P_\omega^2} \tag{2.25}$$

Equation 2.25 can be simplified using considerations of the setup. The same fundamental frequency and optics setup was used for both the sample and the reference materials; therefore the quantity in brackets is identical for both and can be dropped. Furthermore, the same fundamental intensity was used and thus can also be eliminated. These simplifications

result in the ratio of second harmonic powers given in 2.26.

$$\frac{P_{2\omega_s}}{P_{2\omega_r}} = \frac{n_{\omega_r}^2 n_{2\omega_r}}{n_{\omega_s}^2 n_{2\omega_s}} \frac{L_{c_s}^2(0)}{L_{c_r}^2(0)} \frac{d_s^2}{d_r^2} \tag{2.26}$$

A final rearrangement gives the expression for the d_{ij} coefficient given in 2.27.

$$d_s = d_r \sqrt{\frac{P_{2\omega_s}}{P_{2\omega_r}}} \frac{L_{c_r}(0)}{L_{c_s}(0)} \frac{n_{\omega_s}}{n_{\omega_r}} \sqrt{\frac{n_{2\omega_s}}{n_{2\omega_r}}} \tag{2.27}$$

In expression 2.27, d_r is a component of the d coefficient tensor of the reference material, $P_{2\omega_s}$ and $P_{2\omega_r}$ are the measured peaks of the fringe envelopes. L_{c_s} and L_{c_r} are the previously calculated coherence lengths, and n_{ω_s}, n_{ω_r}, $n_{2\omega_s}$, and $n_{2\omega_s}$ are the indices of refraction at the fundamental and second harmonic, respectively.

2.2.2 Third Harmonic Measurements

In a fashion similar to that used for the second harmonic measurements, the third order nonlinear coefficients of many materials can also be theoretically predicted and measured. The expression for third harmonic generation in a bulk nonlinear crystal is given in equation 2.28. [30]

$$P_{3\omega} = \left[\frac{12L^2\omega^2}{\epsilon_o^2 c^4 A^2}\right] \frac{1}{n_\omega^3 n_{3\omega}} C_{ij}^2 P_\omega^3 sinc^2\left(\frac{\Delta k}{2}L\right) \tag{2.28}$$

As before, L is the crystal thickness, ω is the frequency of the fundamental beam, A is the "spot size" (πw_o^2 for a gaussian beam), C_{ij} is the third order nonlinear coefficient, P_ω is the incident power, and Δk is the phase mismatch ($\Delta k = 3k_\omega - k_{3\omega}$).

The setup for conducting the third harmonic measurements is identical to that used for second harmonic experiments with the appropriate filters replaced. The same approximations used to simplify the second harmonic expression may also be used here. Thus, the expression for transmitted third harmonic power from a bulk nonlinear crystal may be given in 2.29.

$$P_{3\omega} = \left[\frac{12L^2\omega^2}{\epsilon_o^2 c^4 A^2}\right] \frac{1}{n_\omega^3 n_{3\omega}} C_{ij}^2 P_\omega^3 T_\omega(\theta) T_{3\omega}(\theta) sinc^2\left(\frac{\Delta k}{2}L\right) \tag{2.29}$$

$T_\omega(\theta)$ and $T_{3\omega}(\theta)$ are transmission factors serving the same purpose as those for the second harmonic, where instead of second harmonic the third harmonic transmission factor

has been substituted. These transmission factors are given in equations 2.30 and 2.31 where the internal angle substitutions have already been made.

$$T_\omega(\theta) = \frac{2\cos\theta}{n_\omega \cos\left[\arcsin\left(\frac{\sin\theta}{n_\omega}\right)\right] + \cos\theta} \tag{2.30}$$

$$\begin{aligned} T_{3\omega}(\theta) = {} & \frac{2n_{3\omega}\cos\left[\arcsin\left(\frac{\sin\theta}{n_{3\omega}}\right)\right]}{\left(n_{3\omega}\cos\left[\arcsin\left(\frac{\sin\theta}{n_{3\omega}}\right)\right] + \cos\theta\right)^3} \times \\ & \left(\cos\theta + n_\omega \cos\left[\arcsin\left(\frac{\sin\theta}{n_\omega}\right)\right]\right) \times \\ & \left(n_\omega \cos\left[\arcsin\left(\frac{\sin\theta}{n_\omega}\right)\right] + n_{3\omega}\cos\left[\arcsin\left(\frac{\sin\theta}{n_{3\omega}}\right)\right]\right) \end{aligned} \tag{2.31}$$

To obtain the expression for total third harmonic power transmitted through the crystal, the argument of the $sinc(x)$ function may be simplified. The same definition for coherence length may be used as given in equation 2.9, but expressed for third harmonic phase mismatch, given in 2.32.

$$L_c \approx L_c(0) = \frac{\pi}{\Delta k} = \frac{\lambda}{6(n_{3\omega} - n_\omega)} \tag{2.32}$$

Finally, the same simplifications used previously result in an expression for the total transmitted third harmonic power as a function solely of the angle of incidence, θ, given in 2.33.

$$P_{3\omega}(\theta) = \left[\frac{16}{3\epsilon_o^2 c^2 \pi^2 w_o^4}\right] \frac{1}{n_\omega^3 n_{3\omega}(n_\omega - n_{3\omega})^2} C_{ij}^2 P_\omega^3 T_\omega(\theta) T_{3\omega}(\theta) \sin^2(\psi(\theta)) \tag{2.33}$$

where

$$\psi(\theta) = \frac{\pi}{2}\frac{L}{L_c(0)}\frac{1}{\cos\left[\arcsin\left(\frac{\sin\theta}{n_\omega}\right)\right]} \tag{2.34}$$

$$T_\omega(\theta) = \frac{2\cos\theta}{n_\omega \cos\left[\arcsin\left(\frac{\sin\theta}{n_\omega}\right)\right] + \cos\theta} \tag{2.35}$$

$$T_{3\omega}(\theta) = \frac{2n_{3\omega}\cos\left[\arcsin\left(\frac{\sin\theta}{n_{3\omega}}\right)\right]}{\left(n_{3\omega}\cos\left[\arcsin\left(\frac{\sin\theta}{n_{3\omega}}\right)\right]+\cos\theta\right)^3}\times$$
$$\left(\cos\theta + n_\omega\cos\left[\arcsin\left(\frac{\sin\theta}{n_\omega}\right)\right]\right)\times$$
$$\left(n_\omega\cos\left[\arcsin\left(\frac{\sin\theta}{n_\omega}\right)\right]+n_{3\omega}\cos\left[\arcsin\left(\frac{\sin\theta}{n_{3\omega}}\right)\right]\right) \tag{2.36}$$

This expression for third harmonic power predicts the shape of a given thickness of a material. However, to calculate an element of the C coefficient tensor from experimental data, this expression, in simplified form, must be used in a relative measurement. In this case the coherence length is again calculated from the minima of the experimental curve and the C_{ij} coefficient from the ratio of peak powers of the test material and a reference. The same simplifications used for the second harmonic power apply equally well for the third harmonic tests. The coherence length is therefore given identically by equation 2.22, rewritten here.

$$L_c(0) = \frac{\tilde{L}}{2}\left(\frac{1}{\cos\left[\arcsin\left(\frac{\sin\theta_{m+1}}{n_\omega}\right)\right]}-\frac{1}{\cos\left[\arcsin\left(\frac{\sin\theta_m}{n_\omega}\right)\right]}\right) \tag{2.37}$$

The expression for the third harmonic power can be simplified using the same assumptions as were used for the second harmonic expression to yield equation 2.38.

$$P_{3\omega} = \left[\frac{48\omega^2}{\epsilon_o^2 c^4\pi^2 w_o^4\Delta k^2}\right]\frac{1}{n_\omega^3 n_{3\omega}}C_{ij}^2 P_\omega^3 T_\omega(\theta)T_{3\omega}(\theta) \tag{2.38}$$

A final substitution can be made for the coherence length using $L_c(0) = \frac{\pi}{\Delta k}$, which results in 2.39.

$$P_{3\omega} = \left[\frac{48\omega^2}{\epsilon_o^2 c^4\pi^4 w_o^4}\right]\frac{1}{n_\omega^3 n_{3\omega}}L_c^2(0)C_{ij}^2 P_\omega^3 T_\omega(\theta)T_{3\omega}(\theta) \tag{2.39}$$

To obtain a value for the C_{ij} coefficient, the ratio of peak powers for a sample and a reference material is used. The two transmission factors are assumed to be similar in magnitude for both materials at normal incidence and are thus dropped from the expression. Thus, the ratio is given in expression 2.40, where the s subscript indicates sample and r indicates reference.

$$\frac{P_{3\omega_s}}{P_{3\omega_r}} = \frac{\left[\frac{48\omega^2}{\epsilon_o^2 c^4 \pi^4 \omega_o^4}\right] \frac{1}{n_{\omega_s}^3 n_{3\omega_s}} L_{c_s}^2(0) c_s^2 P_\omega^3}{\left[\frac{48\omega^2}{\epsilon_o^2 c^4 \pi^4 \omega_o^4}\right] \frac{1}{n_{\omega_r}^3 n_{3\omega_r}} L_{c_r}^2(0) C_r^2 P_\omega^2} \tag{2.40}$$

Equation 2.40 may be simplified. The same fundamental frequency and intensity are used in an identical setup for the reference and sample experiments. Therefore, the entire term in brackets may be dropped as can the incident fundamental intensity. These simplifications result in expression 2.41.

$$\frac{P_{3\omega_s}}{P_{3\omega_r}} = \frac{n_{\omega_r}^3 n_{3\omega_r}}{n_{\omega_s}^3 n_{3\omega_s}} \frac{L_{c_s}^2(0)}{L_{c_r}^2(0)} \frac{C_s^2}{C_r^2} \tag{2.41}$$

Finally, rearranging the simplified expression yields one for calculating the C_{ij} coefficient from measured data given in 2.42.

$$C_s = C_r \sqrt{\frac{P_{3\omega_s}}{P_{3\omega_r}}} \frac{L_{c_r}(0)}{L_{c_s}(0)} \left(\frac{n_{\omega_s}}{n_{\omega_r}}\right)^{\frac{1}{2}} \sqrt{\frac{n_{3\omega_s}}{n_{3\omega_r}}} \tag{2.42}$$

In expression 2.42, C_r is a component of the C coefficient tensor of the reference material, $P_{3\omega_s}$ and $P_{3\omega_r}$ are the measured peaks of the fringe envelopes. L_{c_s} and L_{c_r} are the previously calculated coherence lengths, and n_{ω_s}, n_{ω_r}, $n_{3\omega_s}$, and $n_{3\omega_s}$ are the indices of refraction at the fundamental and third harmonic, respectively.

2.3 Alternative Characterization Methods

In addition to the powder test and the Maker Fringe test, some new methods for characterizing the nonlinear optical coefficients of various materials have been recently proposed. These new methods hold out the promise of being able to accurately quantify the optical coefficients using an absolute measurement as opposed to a relative one, while avoiding the complexities of three and four–wave mixing experiments. Two such methods are the z-scan technique and the pump–probe test.

2.3.1 The Z-Scan Technique

The z-scan technique is a method used to measure the nonlinear refractive index of a single crystal sample. [11] The nonlinear refractive index, n_2, is defined as shown in equation 2.43, in relation to the total refractive index of the material.

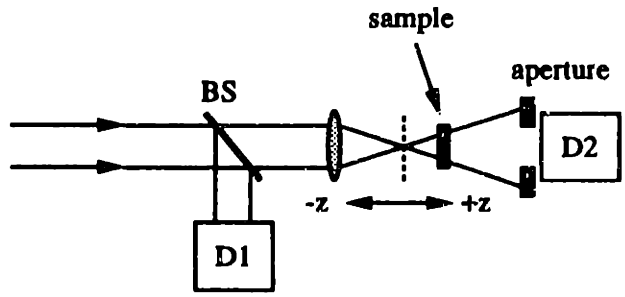

Figure 2-4: Z-scan configuration

$$n = n_o + n_2 I = n_o + \Delta n_o \tag{2.43}$$

In expression 2.43, n_o is the linear refractive index, and I is the incident intensity. The configuration used to perform this test is shown in figure 2-4, where the normalized transmittance, T, is given by $\frac{D_2}{D_1}$. The z-scan technique allows determination of both the sign and magnitude of the nonlinear refractive index. The sign of n_2 comes from the self-focusing or self-defocusing effects of the nonlinear medium on the beam. For a medium with a positive nonlinear refractive index placed in front of the original focus, the focal point of the beam will be shifted toward the medium resulting in a decrease in the normalized transmittance. Furthermore, this same medium placed after the original focus, causes the beam to focus slightly more than with no medium resulting in an increased transmittance. Thus, as the medium traverses a path starting in front of the focus, through, and then beyond the focus, the value of T drops to a valley, then rises through a peak before normalizing back to one. This pattern for the transmittance is shown in figure 2-5.[11]

The opposite effects are observed for a medium with a negative nonlinear refractive index. The peak in the transmittance occurs first and then the valley follows. Recognition of this pattern reveals the sign of n_2.

The magnitude of the nonlinear refractive index can also be calculated from z-scan measurements. To simplify the calculations, the experiment is typically performed under the conditions where the medium can be considered thin. That is, the sample length is small enough, such that changes in the beam diameter within the sample due to diffraction or refraction can be neglected.[11] With these assumptions, the phase change, $\Delta\phi$, at the exit surface of the material may be given by 2.44. [12]

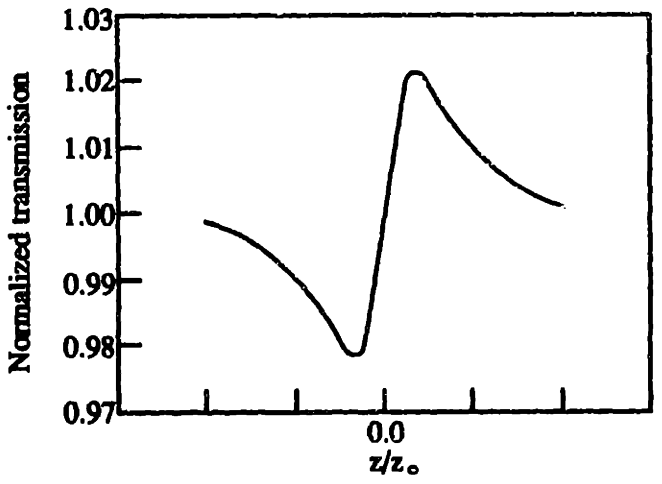

Figure 2-5: Normalized transmittance of positive n_2 material

$$\Delta\phi = \frac{\Delta\Phi_o}{1+\frac{z^2}{z_o^2}} e^{-\frac{2r^2}{w^2(z)}} \tag{2.44}$$

where

$$\Delta\Phi_o = \frac{2\pi}{\lambda}\Delta n_o \frac{1-e^{-\alpha L}}{\alpha} \tag{2.45}$$

z_o is the location of the beam waist, z is the position relative to the waist, α is the absorption coefficient, L is the sample thickness, $w(z)$ is the beam waist at a position z, r is the radial component of the gaussian beam, and $\Delta\Phi_o$ is the phase distortion. The phase distortion can be linked to the measured normalized transmittance as shown in equation 2.46. [12]

$$\Delta T_{p-v} = T_p - T_v \approx 0.405|\Delta\Phi_o| \ , \ \ |\Delta\Phi_o| \leq \pi \tag{2.46}$$

Δn_o can be related to n_2 via the relation shown in 2.43. The nonlinear refractive index can easily be transformed into a rough approximation of the third order nonlinear coefficient, C_{ij} or $\chi^{(3)}$, via equation 2.47. [28]

$$\chi^{(3)} \approx \epsilon_o c n_o n_2 \tag{2.47}$$

In the expression for $\chi^{(3)}$, n_o is the linear refractive index and can be obtained from a simple Brewster's angle measurement, and c is the speed of light in vacuum.

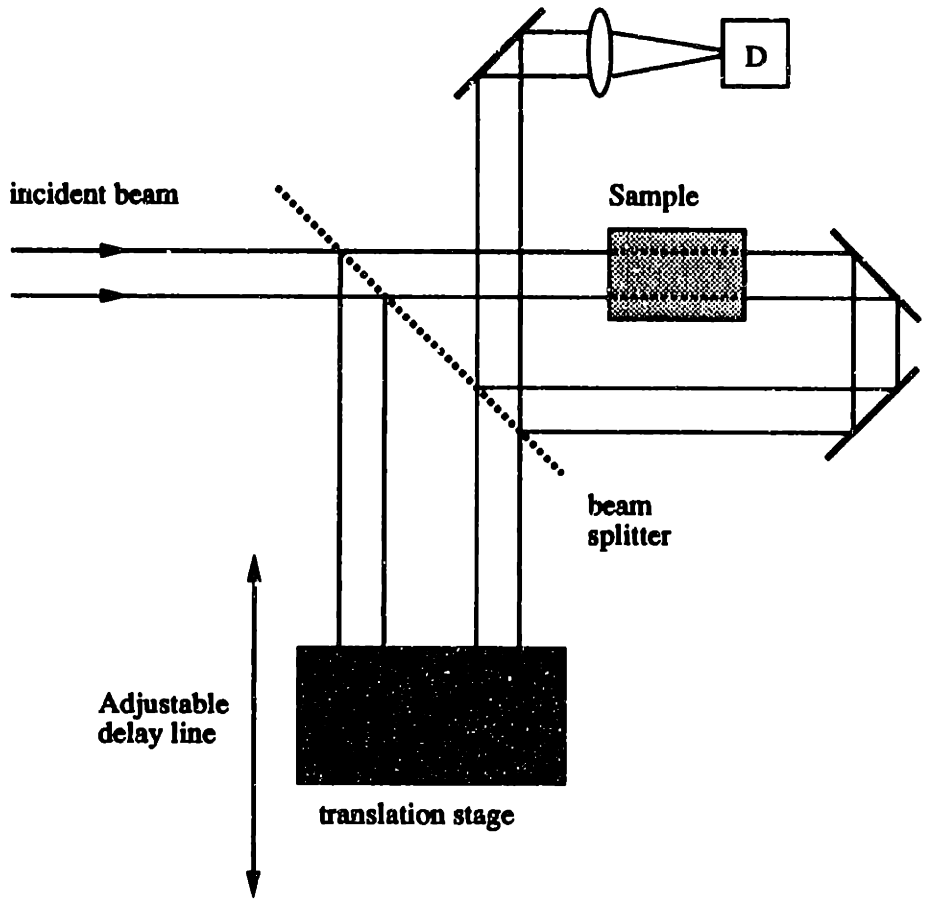

Figure 2-6: Pump–probe test configuration

2.3.2 Pump–probe Tests

The pump–probe test is conducted in a fashion similar to that of the z-scan measurements. However, in this case an initial pump pulse initiates the change in the refractive index due to n_2. A probe pulse is then incident on the sample and the phase change due to the alteration of the refractive index is measured. From these measurements a third order nonlinear coefficient can be calculated.

The pump–probe tests use an interferometric means to generate a phase shift that can be measured. By adjusting the translation stage and altering the delay of the probe pulse the phase shift due to material nonlinearities can be measured. The phase shift can then be converted to a value for the nonlinear refractive index (dependent upon the polarization), from which various elements of the $\chi^{(3)}$ tensor can be calculated.[10]

Chapter 3

Experimental Procedure

The procedure used to take the measurements of the nonlinear materials was broken down into three separate areas. The first part of the experiment was to prepare the samples. For the powder tests, a powder portion of each sample had to be ground and placed in a transparent container made from fused silica. The samples for the Maker Fringe tests were single crystals of the materials grown from solution and mounted on fused silica slides. The second part of both the powder tests and the Maker Fringe tests was characterizing the experimental setup to account for any anomalies due to the optics that were used. Finally, the experiments were run from computer for improved accuracy, requiring software to control the experiments.

3.1 Powder Sample Preparation

Prior to preparing any of the powder samples, the glass containers were constructed. These containers were created from a fused silica slide, three fused silica cover slips, and an ultraviolet epoxy that was index matched to the glass. The first step was to bond one of the cover slips to the glass slide, flush with an edge. Enough epoxy was applied so that there were no gaps between the cover slip and the slide. A second cover slip was placed on the glass slide, approximately five millimeters down from the first, and bonded in the same way. The entire unit was then placed under a longwave ultraviolet light to cure. The uncovered vessel is shown in figure 3-1.

The powder samples tested here were based on the stilbene and stilbazole chromophores, as mentioned earlier. These materials were produced by a group of organic chemists at the

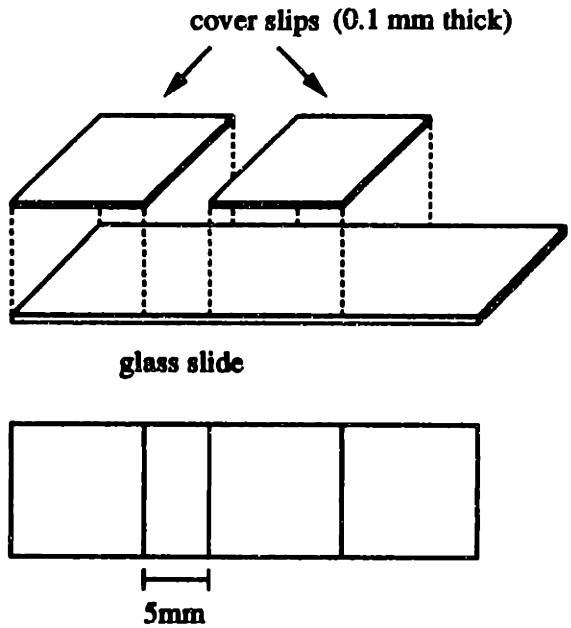

Figure 3-1: Uncovered container for powder tests

General Electric Corporate Research and Development Center.[3] The resultant powders were then used as the source material for the powder tests. The various samples prepared and tested are shown in appendix B along with reference numbers that will be used throughout the discussion of the results. Approximately 20 to 30 grams of a given sample were placed in a mortar. The sample was then ground until no more visible changes in particle size were noticed with continued grinding. A small amount of the pulverized material was then placed in the 5 mm gap of a pre-prepared, uncovered container. The material filled the gap in the vessel, but formed a thin enough layer so that the top cover slip laid perfectly flat. The epoxy was applied in a circle around the sample, the cover slip was placed on top, and the entire vessel with the sample was placed under the ultraviolet light to cure; after the curing process the sample was tagged with a reference number and recorded. The entire process resulted in an airtight container with approximately 30 to 40 square millimeters of surface area for beam exposure. The final container is shown in figure 3-2.

There were some intricacies to note with regards to the powder sample preparation. In some cases, the materials were particularly hygroscopic. These samples underwent a visible phase change from an anhydrous form to an hydrate during the grinding process, and therefore were re-prepared without grinding. In some of the most extreme cases, the samples were prepared in an environment less humid than the ambient air, such as a nitrogen-filled

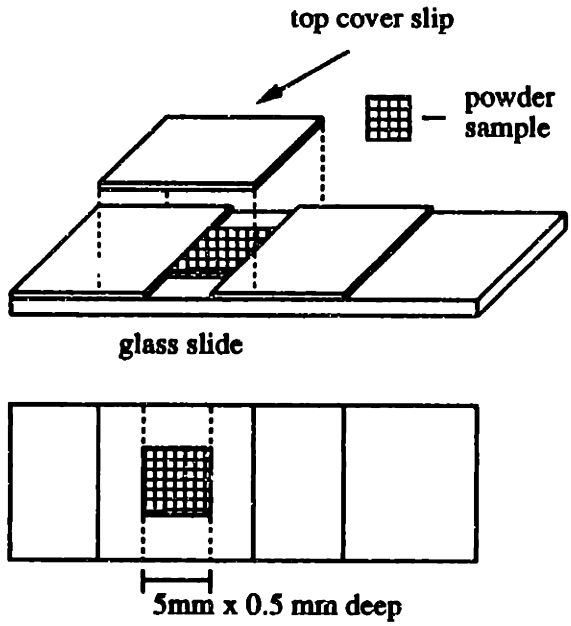

Figure 3-2: Final container for powder tests with powder sample

glove box. However, in all cases both the hydrate and the anhydrate materials were kept and tested.

3.2 Crystal Growth and Mounting

The Maker Fringe tests were conducted using single crystals of the materials. These crystals were grown from a saturated solution by carefully controlling the temperature. First, a double–walled glass vessel was filled with methanol and connected to a constant temperature bath, circulating water between the first and second walls of the container. The water was heated, and consequently so was the methanol. The organic material to be grown was added, in powder form, to the methanol until the solution became saturated. The vessel was then sealed with a seeder string immersed in the center. The temperature of the bath was slowly lowered ($\frac{1}{2}^\circ$ to 1° per day) to allow a slow crystallization process. The process was continued over a period of one to two weeks; at the point where no further substantial growth was noted, the crystals were harvested from solution.

It was found that this process tended to be inefficient in utilizing the available material in solution. The inefficiency was a result of depletion zones that formed around the crystal surfaces – areas where the organic material concentration was markedly lower than the

surrounding solution. To correct for this problem, a dc motor was used to slowly rotate the seeder string back and forth, preventing the generation of depletion zones in the solution.

The harvested crystals were placed in glass containers, which were then placed inside vacuum chambers filled with a highly water–absorbent material (for example dri-rite). The purpose here was to dry any methanol still on the crystal surfaces and to prevent any ambient water absorption by some of the more hygroscopic materials. Following drying, each crystal was mounted onto a fused silica slide.

The crystals were mounted on the slides using an epoxy that was cured via exposure to longwave ultraviolet light. However, the bond material was sensitive to the laser light being used, damaging easily upon exposure. Therefore, the optical path through the crystals had to be free of any epoxy. The crystals were mounted by placing a drop of bond on the slide and manipulating the very corner of a crystal into it. With the crystal mounted, the slide and crystal were placed under the ultraviolet lamp to cure. Once the epoxy had sufficiently hardened, the mounted sample was placed back into the covered vacuum chambers until the tests were run.

3.3 Experimental Setup

The powder tests and Maker Fringe experiments were run using an identical optics setup. However, due to differences in the tests, different devices were needed for mounting and manipulating the samples. The signal detection and amplification schemes where basically the same for both measurements. Finally, the tests were run via computer and required slightly different software for each.

3.3.1 Optics Layout

The optics setup used for the measurements is shown in figure 3-3. The same setup was used for both types of experiments. The linearly–polarized, fundamental beam of a 20 Hz, unseeded, Q-switched Nd:YAG laser, at a wavelength of 1.064 μm, was Raman shifted out to 1.907 μm. A 60 cm path–length cell pressurized to 500 psi with high–purity hydrogen gas, H_2, provided high–order Stokes and anti-Stokes Raman shifted light, collinear with the incident beam (for a discussion of the Raman scattering process the reader is referred to appendix A). A Pellin broca prism and circular aperture selected the 1.907 μm beam

from the output of the cell. A calcite polarizer provided the proper polarization to carry out the tests. In addition, for both the Maker Fringe and powder tests a reference arm was used to normalize out pulse–to–pulse fluctuations of the laser. A plane–parallel silicon window was placed in the beam path at an angle of incidence of 40°. The fresnel reflection for a transverse electric field was then used as the input beam for the reference arm; at the given angle of incidence the ratio of transmitted to reflected intensity was 1.5 ($T_\perp$ = 0.6; $R_\perp$ = 0.4). The material in the reference arm was a powder sample of dimethylamino stilbazolium tosylate (DAST) in a fixed mount. DAST was used as a normalizing sample because the second harmonic signal was sensitive to pulse width and energy fluctuations; in addition, the large second harmonic signals produced were easily detected. During the third harmonic tests, the laser intensity was increased. To prevent damage to the DAST sample in the reference arm, a Corning glass filter (optical density 0.92 at 1.907 μm, #5850) was placed in the optical path of the reference arm.

The different measurements provided by each type of test required separate devices for holding and manipulating the samples. The powder test samples were held in a stationary position aligned with the beam incident on a portion of the sample. The Maker Fringe tests, on the other hand, required that the sample be carefully aligned in the beam and rotated. Therefore, the area indicated in figure 3-3 as *sample mount* was different for each test.

3.3.2 Powder Test Mount

The powder tests were conducted under conditions that minimized sample–to–sample fluctuations. To avoid any induced deviations, each sample was held at a rigidly fixed inclination to the beam that did not vary between samples. In addition, the entire spot size of the beam was incident on each sample. These conditions required that the samples be easily interchangeable but that the mount that held them stay fixed in position. To comply with the requirements, a pinch–type filter mount was used. The setup used to hold and manipulate the powder samples is shown in figure 3-4.

To replace samples the pinch was loosened and the current sample removed. The new slide was placed in the filter mount and the pinch was tightened. As mentioned previously, each sample container was prepared in an identical manner; the filter mount was fixed at a given height and inclination to the beam and, therefore, there were no variations in height from sample to sample. Furthermore, the consistency of the height and ease of sample

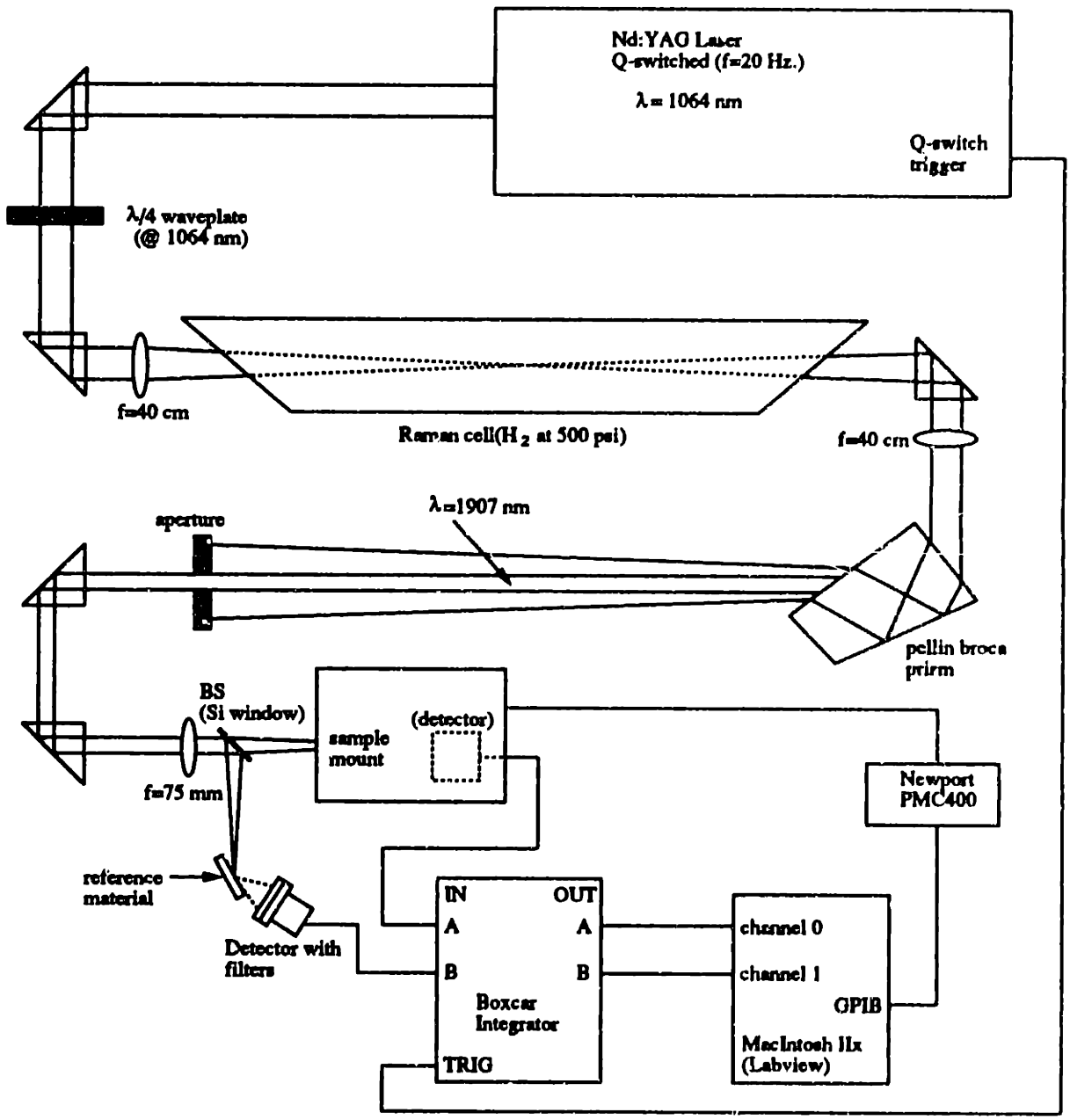

Figure 3-3: Optics setup for powder and Maker Fringe tests

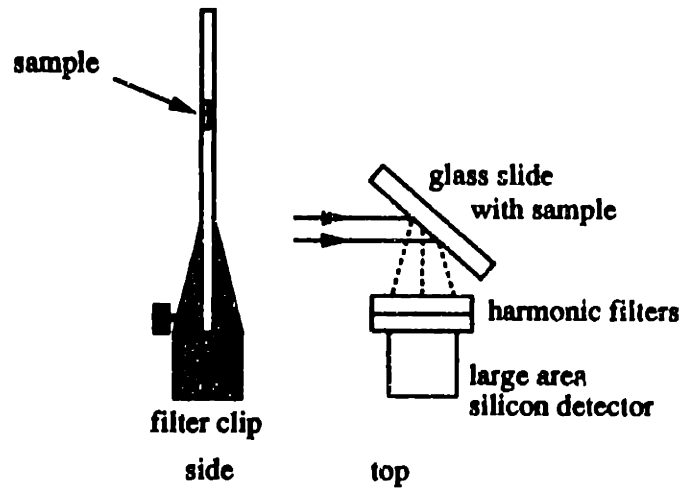

Figure 3-4: Powder sample mount

access guaranteed that the detection scheme remained unchanged from sample to sample.

3.3.3 Maker Fringe Mount

The Maker Fringe tests did not have the rigid sample–to–sample consistency constraints that were placed on the powder tests. However, the sample had to be meticulously aligned and carefully rotated such that the axis of rotation was perpendicular to the beam and the two intersected at the front facet of the crystal. Intersection of the rotational axis and the beam in the bulk of the crystal, or other forms of misalignment, produced nonviable results as the beam tended to walk–off the sample during rotation. In addition, the crystallographic axes had to be aligned with respect to the polarization of the incident beam to avoid any problems with angular dependences in the nonlinear coefficients. Therefore, the sample mount required mobility in all six degrees of freedom, one for rotation and the other five for alignment. The sample mounting device used for the Maker Fringe tests is shown in figure 3-5.

The rotational stage on which the rest of the mount was placed was a Newport Optics series 495 automated rotational stage controlled by a Newport PMC400 controller. The rotation was handled by an Apple Macintosh IIx connected via a general purpose interface bus (GPIB). The stage handled the rotation of the crystal through the incident beam. A three axis, manually controlled, translation stage provided omni–directional positioning, while two cross–connected, manual rotational mounts provided precise control of roll and pitch. The sample was mounted onto the face of rotational stage A (see figure 3-5) via

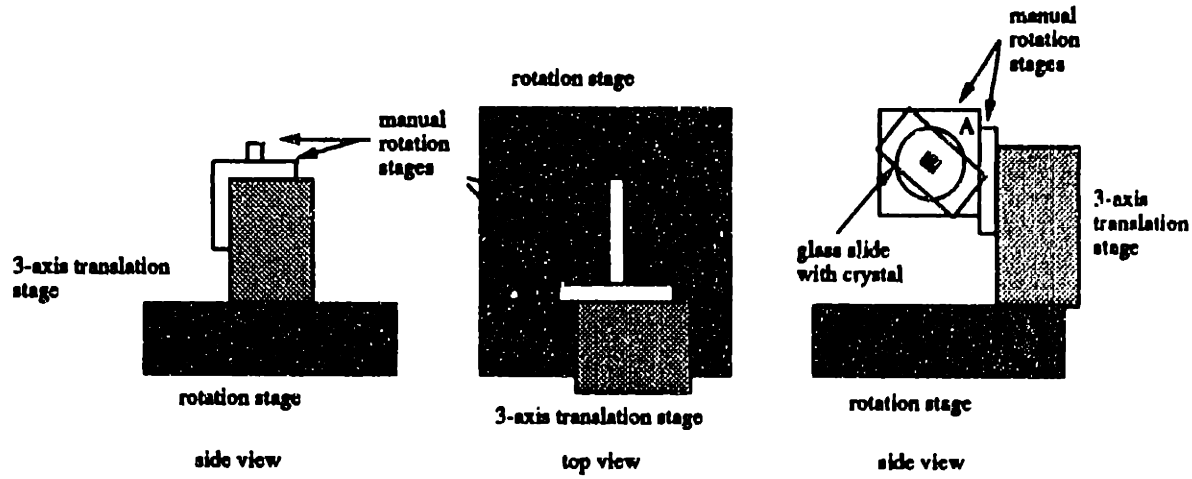

Figure 3-5: Maker Fringe sample mount

adhesive. Each individual sample required only that the alignment be precise with respect to the rotational axis, crystallographic axis, and incident beam; however, sample-to-sample fluctuations in position were not relevant.

3.3.4 Signal Detection and Amplification

The same optical setup was used for tests conducted at the second harmonic, 953.5 nm, and third harmonic, 635.7 nm. Therefore, the detection scheme had to provide significant detection and amplification ability at both wavelengths. In addition, the effects of noise had to be minimized.

Signal detection was provided by zero-biased, large-area (1 cm^2), silicon PIN photodiodes. The signal from the photodiodes was amplified using a low-noise transimpedance amplifier. A two-channel boxcar integrator, triggered off of the laser, sampled the amplified pulses. The voltage outputs of the boxcar integrator were then digitized and collected via an Apple Macintosh IIx computer, running Labview (©National Instruments) software.

The same detection scheme was used for all the experiments conducted. However, in order to select the second or third harmonic signals, glass and interference filters were placed directly in front of the detectors. For second harmonic tests, a short-pass glass filter (Schott RG-9) absorbed the 1.907 μm fundamental beam but transmitted the 953.5 nm signal with 73% efficiency. A bandpass interference filter centered at 950 nm selected the second harmonic signal. For third harmonic tests, a bandpass glass filter (Schott KG-3) absorbed both the fundamental and second harmonic signals, but transmitted the 635.7

signal with 71% efficiency. A bandpass interference filter centered at 633 nm was then used to discriminate the third harmonic signal from multi-photon fluorescence.

3.4 Data Acquisition

The collection of the data from the boxcar integrator was handled via an Apple Macintosh IIx computer, running Labview software (©National Instruments). The software, however, was slightly different for each test. The powder tests required simple averaging over a series of laser pulses. The Maker Fringe tests, on the other hand, required averaging over a series of pulses while simultaneously handling stage rotation. In both cases, the raw data was analyzed to obtain usable information.

3.4.1 Powder Tests

The powder tests required a simple averaging algorithm. The software allowed any number of pulses to be averaged. For the work conducted here, 1000 pulses were averaged. Each channel of the boxcar integrator (the sample and the DAST reference) was read simultaneously. The channels were sampled at one-half of the Q-switch frequency of the laser to insure that each pulse was separate and independent of any previous pulses. (in this case only every other pulse was recorded). The voltage of the sample arm was divided by that of the reference arm to normalize out fluctuations. The software then summed the arbitrary intensity-dependent voltages returned over 1000 pulses and divided by 1000. The software returned a number representative of the measured second or third harmonic intensity generated by a particular sample.

The powder efficiencies of the samples were calculated from measurements of a material to which the numbers could be referenced. For the second harmonic measurements, the samples were referenced to Urea; for third harmonic tests, the signals were referenced to dimethylamino nitrosilbene (DANS). Urea and DANS were tested periodically over the course of the powder measurements to maintain a consistent value for referencing. Once the raw data had been collected the arbitrary intensity-dependent numbers returned by the software for each sample were divided by those returned for Urea or DANS (depending on the second or third harmonic test being run). The ratio of sample to reference gave a powder efficiency for the material.

3.4.2 Maker Fringe Tests

The Maker Fringe tests required a slightly more complex program than did the powder tests. The same averaging routine was used, as pulses were read off both channels of the boxcar integrator simultaneously, summed and normalized. The sampling was again carried out at one–half of the Q-switch frequency, averaging over some number of pulses. However, in addition to averaging the pulses, the software also had to drive the rotational stage and keep track of the degree of rotation at which the current sampling was taking place.

The controls for the tests had to be flexible to allow the speed and accuracy of the test to be manipulated. The software allowed any number of pulses to be averaged; fifty pulses were averaged here. The test could be run from any initial inclination to the beam to any final inclination, with varying incremental step size (0.01° to any upper level step size). The software recorded the averaged value and the degree at which that average was taken; the information was dumped into a standard ASCII file.

The d_{ij} coefficients could only be calculated when the measurements of a particular material were compared relative to a substance with a known nonlinear optical coefficient. Therefore, samples were run in pairs. First, a lithium niobate ($LiNbO_3$, d_{33} = 30 pm/V) reference crystal was run, followed by a sample. The analysis of the raw data was carried out using the Kaleidagraph software package on an Apple Macintosh IIx. The coherence length of each material was calculated from their respective curves via a second order curve fit to local minima. The ratio of the peak powers was then used to derive the value for the particular tensor component of the **d** coefficient being measured (see chapter 2).

Chapter 4

Results and Analysis

The measurements conducted by both the powder tests and Maker Fringe tests returned raw numbers dependent on the intensity of the second or third harmonic generated by a particular material. However, in both cases the raw data needed some analysis to obtain qualifying results for the second or third harmonic powder efficiencies, or for the various elements of the **d** coefficient tensor.

4.1 Powder Test Data

The powder tests were conducted for two separate wavelengths. The second harmonic tests, at 953.5 nm., were referenced to Urea. The third harmonic measurements, at 635.67 nm., were referenced to DANS. Over fifty different materials were tested based on the stilbene and stilbazole chromophores. Multiple powder efficiencies are reported for compounds exhibiting polymorphism.

The raw data for the second and third harmonic measurements along with the second and third harmonic powder efficiencies are given in tables 4.1 through 4.6. The materials are listed by reference numbers that associate measurements with the specific substances listed in appendix B. The numbers given for Urea(A1) and DANS(A5), are representative of a number of measurements performed over the course of the entire test. The tables are broken down into base chromophore, substituent group, and counterion as classified by the reference numbers.

The accuracy of the powder tests was subject to sizable experimental error. There were large fluctuations in the measurements due to a variety of reasons. The samples were unsized

and the varying particle sizes produced sizable differences in measurements. In addition, the method in which the samples were prepared may have influenced the molecular orientation and resulted in altered intensities. Furthermore, fluctuations in the output energy of the laser played a significant role in restricting experimental accuracy. Taking into account the sources of experimental error as compared with other recent measurements made at other locations[2][21], the powder test results are valid to within ±15%.

Table 4.1: Organic reference compounds

Ref. No.	Material	SHG Data (mV)	SHG Eff.	THG Data (mV)	THG Eff.
A1	Urea	0.031	1	0.0	0.0
A2	MNA	2.973	100	0.5	13
A3	MNMA	0.651	20	0.044	1.1
A4	Trimons	0.0047	0.2	0.025	0.6
A5	DANS	0.008	0.3	0.04	1
A6	4-OH NS	0.010	0.3	0.02	0.5
A7	POM	0.840	30	0.043	1.1

4.2 Maker Fringe Results

The Maker Fringe tests were conducted for second harmonic measurements only. In addition, due to the difficulty of obtaining single crystals of sufficient quality, only the d_{11} and d_{12} components were measured for dimethylamino stilbazolium tosylate (DAST) relative to a lithium niobate reference.

4.2.1 Lithium Niobate

The two tensor components of the nonlinear optical coefficient were measured relative to a 1 mm thick, x–cut single crystal of lithium niobate ($LiNbO_3$), shown in figure 4-1.

Lithium niobate crystalizes in trigonal space group C_{3v}, point group $3m$.[33] The second order nonlinear optical coefficient may be given by the contracted notation tensor given in 4.1.

$$\begin{pmatrix} 0 & 0 & 0 & 0 & d_{15} & -d_{22} \\ -d_{22} & d_{22} & 0 & d_{15} & 0 & 0 \\ d_{31} & d_{31} & d_{33} & 0 & 0 & 0 \end{pmatrix} \tag{4.1}$$

Table 4.2: 1-N–Methyl Stilbazolium salts powder results

Ref. No.	SHG Data(mV)	SHG eff.	THG Data(mV)	THG Eff.
B1	0.0	0.0	0.03	0.8
B2	25.6	830	0.46	12
B3	29.4	950	1.61	40
B4	6.45	210	1.02	26
B5	0.002	0.1	0.025	0.6
B6	7.13	230	0.28	7
B7	6.3	200	0.60	15
B8	1.55	50	0.092	2
B9	31.1	960	8.1	200
B10	0.06	2	0.0	0.0
B11	82	2600	2.2	55
B12	9.93	310	0.92	23
B13	0.004	0.1	0.0	0.0
B14	0.0	0.0	0.005	0.1
B15	22.4	700	1.24	31
B16	2.82	91	0.18	5
B17	8.84	290	0.072	2
B18	2.26	73	0.09	2
B19	9.3	300	1.84	50
B20	3.88	125	0.32	10
B21	6.36	205	1.96	50
B22	8.31	270	2.88	70
B23	4.12	135	0.12	3
B24	0.021	0.7	0.02	0.5
B25	0.16	5	0.0	0.0
B26	0.004	0.1	0.0	0.0
B27	0.0	0.0	0.017	0.4
B28	0.0	0.0	0.0	0.0
B29	0.0	0.0	0.0	0.0
B30	0.004	0.1	0.024	0.6
B31	0.01	0.3	0.0	0.0
B32	0.031	1	0.0	0.0
B33	0.017	0.6	0.0	0.0
B34	0.003	0.1	0.0	0.0

Table 4.3: 3-N–Methyl Stilbazolium salts powder results

Ref. No.	SHG Data(mv)	SHG eff.	THG Data(mV)	THG Eff.
C1	0.0	0.0	0.026	0.7
C2	0.003	0.1	0.0027	0.1
C3	0.0	0.0	0.018	0.5
C4	0.0	0.0	0.002	0.1
C5	0.0	0.0	0.0192	0.5
C6	0.003	0.1	0.0	0.0
C7	0.00	0.0	0.031	0.8
C8	0.003	0.1	0.022	0.6
C9	0.0	0.0	0.0	0.0

Table 4.4: 1-O Stilbene salts powder results

Ref. No.	SHG Data(mV)	SHG eff.	THG Data(mV)	THG Eff.
D1	0.089	2.2	0.0	0.0
D2	0.0	0.0	0.0	0.0

Table 4.5: Modified Stilbazole salts powder results

Ref. No.	SHG Data(mV)	SHG eff.	THG Data(mV)	THG Eff.
E1	0.001	0.3	0.02	0.5
E2	0.0	0.0	0.0	0.0

Table 4.6: General unclassified salts powder eff.

Ref. No.	SHG Data (mv)	SHG Eff.	THG Data (mV)	THG Eff.
F1	0.004	0.1	0.0	0.0
F2	0.24	8	0.0	0.0
F3	0.008	0.3	0.0	0.0
F4	0.007	0.2	0.01	0.3
F5	0.0	0.0	0.0	0.0
F6	0.0	0.0	0.0	0.0
F7	0.01	0.3	0.0	0.0
F8	0.0	0.0	0.0	0.0

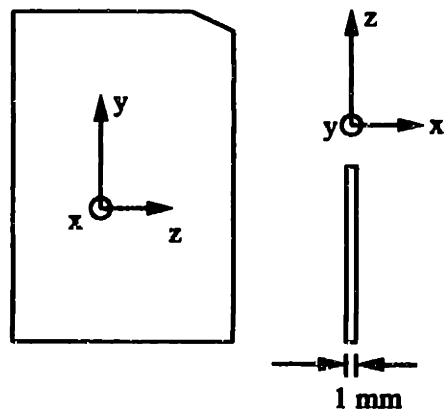

Figure 4-1: X–cut $LiNbO_3$ reference sample

The resulting 3x6 matrix operates on the $\mathbf{E}^2$ column tensor to yield the total polarization vector, **P**. The polarization vector is given in 4.2.

$$\begin{pmatrix} P_x \\ P_y \\ P_z \end{pmatrix} = \begin{pmatrix} 0 & 0 & 0 & 0 & d_{15} & -d_{22} \\ -d_{22} & d_{22} & 0 & d_{15} & 0 & 0 \\ d_{31} & d_{31} & d_{33} & 0 & 0 & 0 \end{pmatrix} \begin{pmatrix} E_x^2 \\ E_y^2 \\ E_z^2 \\ 2E_zE_y \\ 2E_zE_x \\ 2E_xE_y \end{pmatrix} \tag{4.2}$$

The multiplication of the matrices in 4.2 produces the three vector components of the polarization. For lithium niobate, the d_{33} component of the nonlinear coefficient tensor was used as the reference measurement. The only component of the polarization that can be dependent on the d_{33} element is P_z. The resultant z–component of the polarization is given in 4.3.

$$P_z = d_{31}E_x^2 + d_{31}E_y^2 + d_{33}E_z^2 \tag{4.3}$$

Therefore, by illuminating the sample with a z–polarized incident beam ($E_x = E_y = 0$) and measuring the second harmonic output, the d_{33} coefficient can be calculated. The index of refraction for lithium niobate at 1.907 μm, n_ω, is 2.1281; at 953.5 nm, $n_{2\omega}$ is 2.1625. [30] These values give a coherence length of 14.078 μm, from equation 2.10. The theoretical Maker Fringe curve based on the equations given in chapter 2, for a 1 mm thick crystal

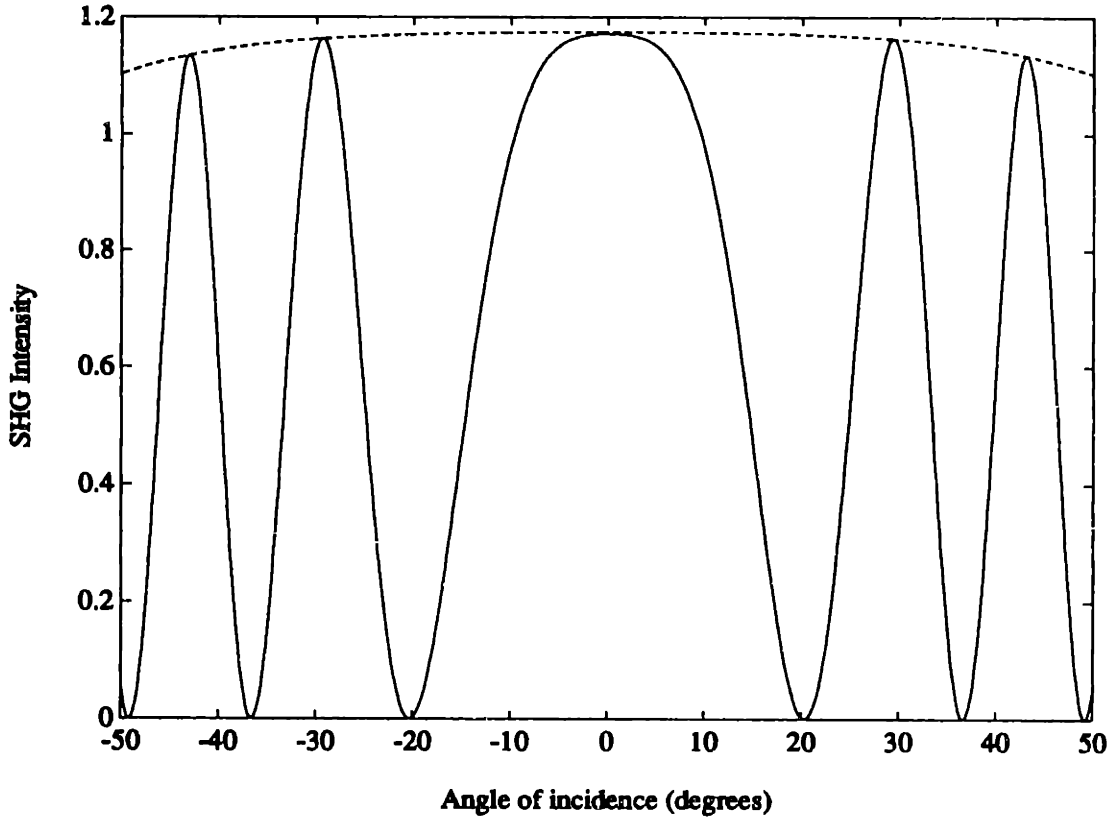

Figure 4-2: Theoretical Maker Fringe curve for $LiNbO_3$ d_{33}

of lithium niobate with the given values for the indices of refraction, the coherence length, and a d_{33} coefficient of 30 pm/V is given in figure 4-2.

An example of the Maker fringe measurements made on lithium niobate is given in figure 4-3. To use the lithium niobate maker fringe data for d_{ij} coefficient calculations, the coherence length needed to be calculated from the observed results. A second order, parabolic, curve fit to each minima yielded the incidence angles given in 4.4. The fringes are symmetric about normal incidence. Therefore, for more accurate determinations of the angles that yield the minima the corresponding positive and negative incidence angles are averaged.

$$\begin{aligned} -\theta_{m+1} &= -36.62^\circ \\ -\theta_m &= -20.45^\circ \\ +\theta_m &= 20.1145^\circ \\ +\theta_{m+1} &= 36.367^\circ \end{aligned} \tag{4.4}$$

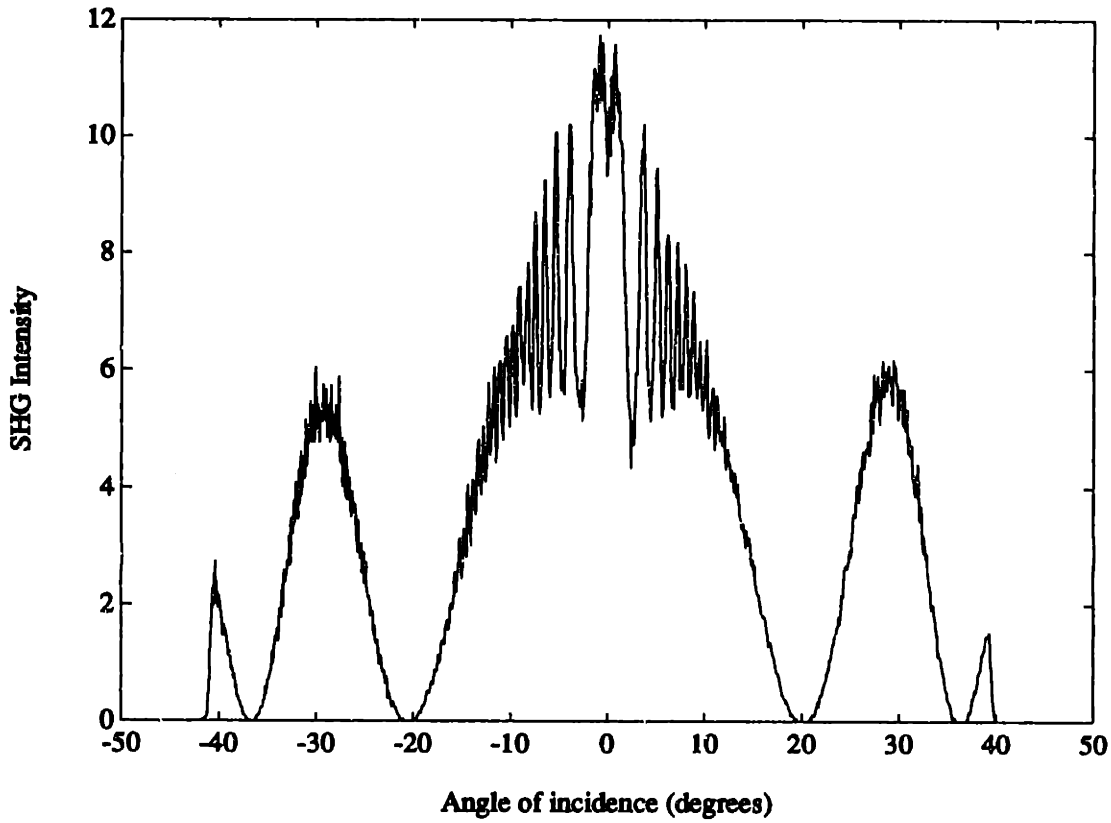

Figure 4-3: Experimental Maker Fringe data for $LiNbO_3$ d_{33}

$$\theta_m = 20.282°$$

$$\theta_{m+1} = 36.49°$$

To obtain a value for the coherence length, the two angles of incidence are substituted into equation 2.22. The substitution yields a coherence length, $L_c(0)$, of 14 μm for a crystal length of 1 mm. This is in good agreement ($\pm$ 1 %) with the expected value of 14.078 μm derived from the indices of refraction. In cases where the data provided more than two minima on each side of normal incidence, more than one coherence length can be calculated. In theory, the coherence length from any two adjacent minima should not differ. However, in practice, small discrepancies (misalignment, crystal imperfections, etc.) can yield slightly varying coherence lengths; and an average of the various lengths is used. Having characterized the reference sample, Maker fringe data on the sample materials can be evaluated.

4.2.2 DimethylAmino Stilbazolium Tosylate (DAST)

The only material for which the Maker Fringe measurements were done was DAST. This material crystallizes in the monoclinic space group Cc, point group m.[2][29] The Cc–m space group–point group configuration has a tensor given in contracted notation by the 3x6 matrix in 4.5.[33]

$$\begin{pmatrix} d_{11} & d_{12} & d_{13} & 0 & d_{15} & 0 \\ 0 & 0 & 0 & d_{24} & 0 & d_{26} \\ d_{31} & d_{32} & d_{33} & 0 & d_{35} & 0 \end{pmatrix} \tag{4.5}$$

The matrix representing the nonlinear optical tensor operates on the $\mathbf{E}^2$ column tensor to yield the components of the polarization vector. The vector multiplication is given in 4.6.

$$\begin{pmatrix} P_x \\ P_y \\ P_z \end{pmatrix} = \begin{pmatrix} d_{11} & d_{12} & d_{13} & 0 & d_{15} & 0 \\ 0 & 0 & 0 & d_{24} & 0 & d_{26} \\ d_{31} & d_{32} & d_{33} & 0 & d_{35} & 0 \end{pmatrix} \begin{pmatrix} E_x^2 \\ E_y^2 \\ E_z^2 \\ 2E_zE_y \\ 2E_zE_x \\ 2E_xE_y \end{pmatrix} \tag{4.6}$$

The crystals, as they were grown, carried the x and y axes in the plane and were normal to z, as shown in figure 4-4. Therefore, the incident field could not be z–polarized and the z–component of the output polarization was zero. The x– and y–directed polarizations simplify to the equations in 4.7 and 4.8.

$$P_x = d_{11}E_x^2 + d_{12}E_y^2 \tag{4.7}$$

$$P_y = 2d_{26}E_xE_y \tag{4.8}$$

Illumination of the DAST crystal with a singularly polarized incident beam will yield only a x–directed output polarization. For a x–polarized incident beam ($E_y = 0$), the output polarization becomes dependent on d_{11} only. Thus by using such an incident polarization and measuring the output second harmonic power, the d_{11} coefficient may be measured. Similarly, using a y–polarized ($E_x = 0$) incident beam will yield measurements for the d_{12}

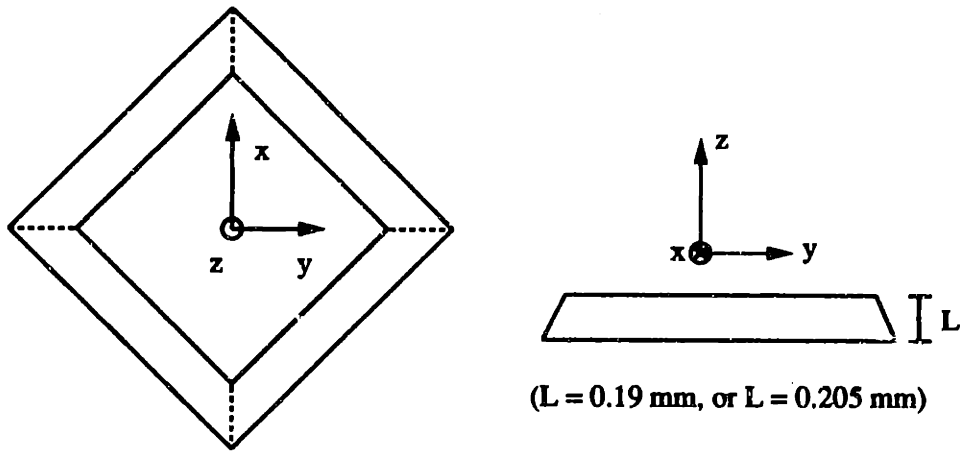

Figure 4-4: DAST crystal sample

coefficient. However, any mixed polarized incident wave yields an output polarization with contributions from d_{11}, d_{12}, and d_{26} that cannot easily be separated.

The DAST crystals used for the Maker Fringe measurements varied in size. The crystal used for the measurement of the d_{11} coefficient was 190 μm thick. The crystal used for the d_{12} measurement was 205 μm thick. The index of refraction, $n_{2\omega,x}$, at the second harmonic wavelength, 953.5 nm., is 2.18 obtained from a Sellmeier fit to previously reported data.[2] The index of refraction of DAST, $n_{\omega,x}$, at the fundamental wavelength is 1.988 determined experimentally from the Maker Fringe data. The measurements of the d_{12} coefficient were carried out with y–polarized incident light. The index of refraction at the fundamental, $n_{\omega,y}$, is 1.9021. The theoretical coherence lengths calculated from 2.10 are $L_c = 2.488$ μm and $_c = 1.716$ μm for d_{11} and d_{12}, respectively. Theoretical Maker Fringe curves based on equation 2.13, for the two tensor components measured, are given in figures 4-5 and 4-6.

An example of the Maker fringe measurements made on DAST, for the d_{11} element, is given in figure 4-7. The first step in calculating the nonlinear coefficient is to compute the coherence length from the minima of the fringes. As with the lithium niobate data, a second order, parabolic, curve fit to each minima yields the incidence angles; the angles are given in 4.9.

$$\begin{aligned} -\theta_m &= -23.9^\circ \\ +\theta_m &= 23.7^\circ \end{aligned} \tag{4.9}$$

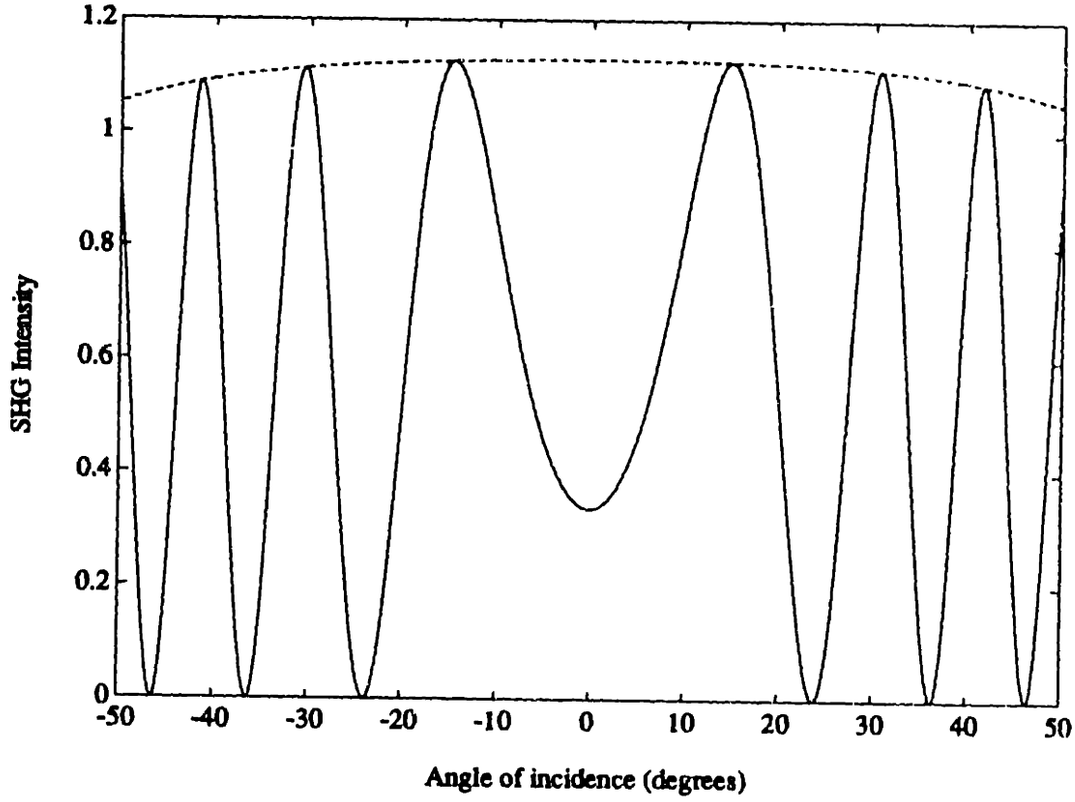

Figure 4-5: Theoretical Maker Fringe curve for DAST d_{11}

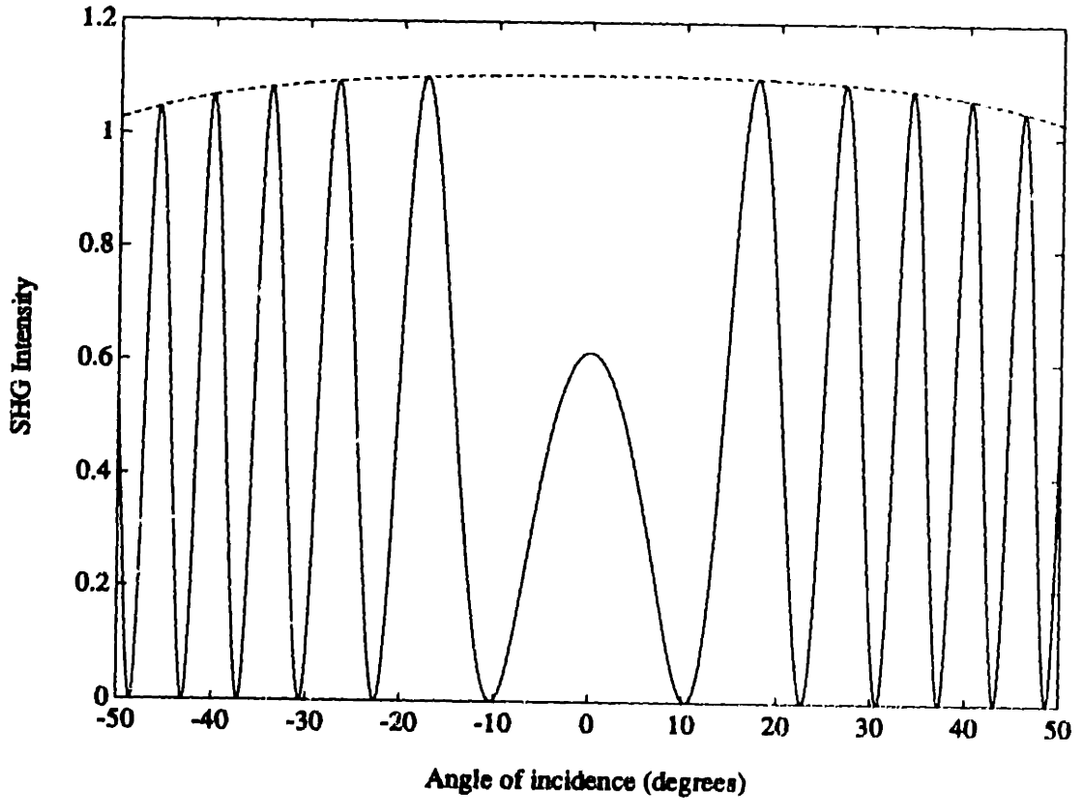

Figure 4-6: Theoretical Maker Fringe curve for DAST d_{12}

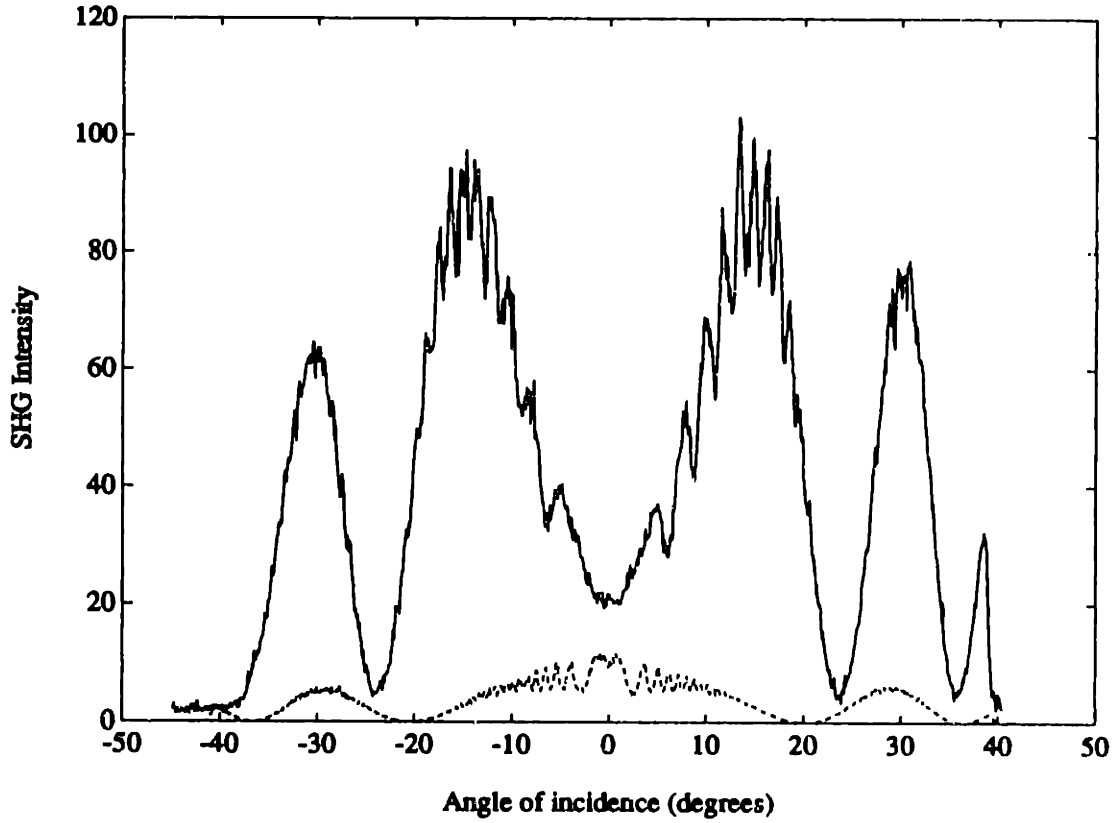

Figure 4-7: Experimental Maker Fringe data for DAST d_{11}

$$+\theta_{m+1} = 35.8°$$

$$\theta_m = 23.3°$$

$$\theta_{m+1} = 35.8°$$

To obtain a value for the coherence length, the two angles of incidence are substituted into equation 2.22 with a crystal length of 190 μm. The substitution yields a coherence length of, $L_c(0)$, of 2.4μm. This is in good agreement ($\pm$ 5 %) with the expected value of 2.488 μm derived from the indices of refraction. The coherence lengths of the DAST and lithium niobate samples may now be used, along with the ratio of the fringe envelopes, to compute the d_{11} coefficient from equation 2.27. The ratio of the peak powers can be measured at approximately 13. For the data, DAST and lithium niobate, given in figure 4-7, the d_{11} coefficient is calculated to be 600 pm/V.

An example of the Maker fringe measurements made on DAST, for the d_{12} element, is given in figure 4-8. A second order, parabolic, curve fit to the minima yields the incidence

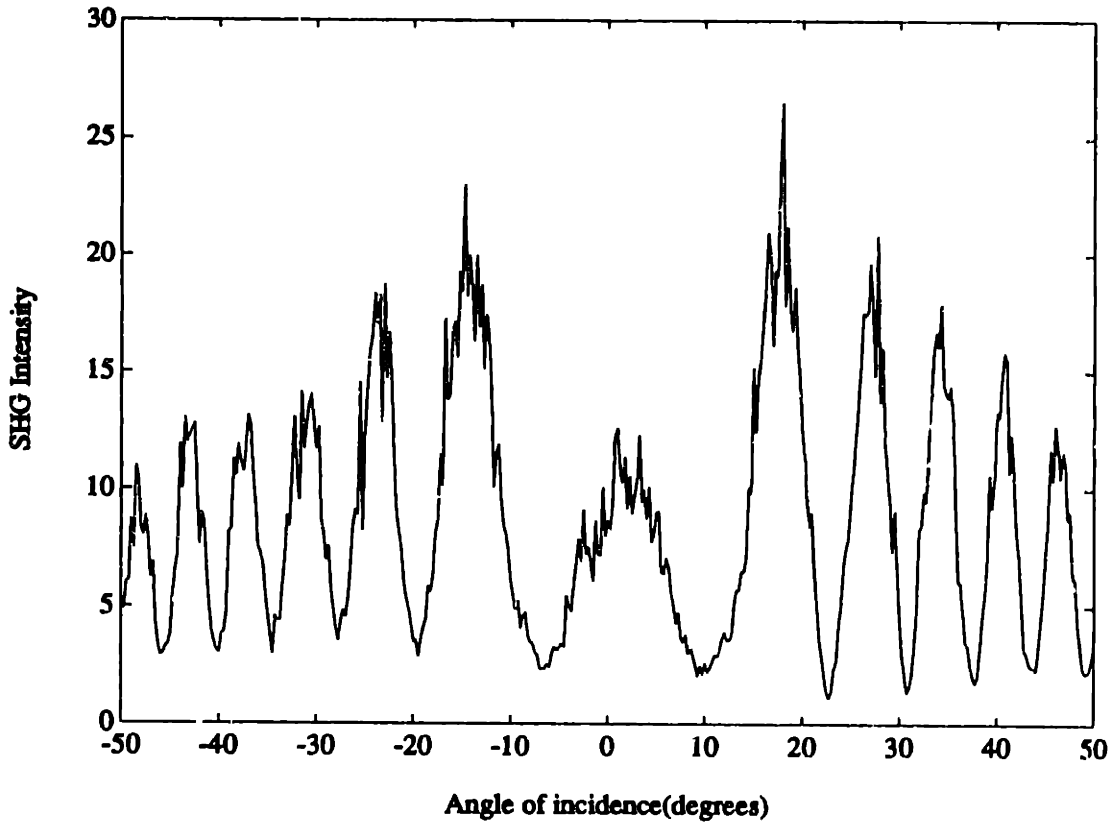

Figure 4-8: Experimental Maker Fringe data for DAST d_{12}

angles given in 4.10.

$$\begin{aligned} \theta_m &= 1.96° \\ \theta_{m+1} &= 21.19° \\ \theta_{m+2} &= 29.243° \\ \theta_{m+3} &= 36.0° \\ \theta_{m+4} &= 41.974° \\ \theta_{m+5} &= 47.47° \end{aligned} \tag{4.10}$$

To obtain a value for the coherence length, the angles of incidence are substituted into equation 2.22. The substitution yields five values for the coherence length given in 4.11. The average of the five calculated values gives an $L_c(0)$ of 1.7 μm. This is in good agreement ($\pm$ 3 %) with the expected value of 1.716 μm derived from the indices of refraction.

$$
\begin{aligned}
L_{c1} &= 1.69\mu m \\
L_{c2} &= 1.71\mu m \\
L_{c3} &= 1.72\mu m \\
L_{c4} &= 1.65\mu m \\
L_{c5} &= 1.64\mu m
\end{aligned}
\tag{4.11}
$$

The coherence lengths of the DAST and lithium niobate sample may now be used, along with the ratio of the fringe envelopes, to compute the d_{12} coefficient from equation 2.27. The ratio of the peak powers was measured at approximately 22 against a lithium niobate sample run just prior. For the data, DAST and lithium niobate, given in figure 4-7, the d_{12} coefficient is calculated to be 215 pm/V. A number of measurements were made for the d_{11} and d_{12} coefficients. The remaining sets of measurements are given in appendix C. Table 4.7 gives the values for the coherence length and the various tensor components of the nonlinear optical coefficient for each set of measurements in appendix C. Various sources of experimental error in the optics setup and crystal growth process lead to an accuracy of $\pm$ 20%

Table 4.7: DAST Maker Fringe results

Figure	$L_c(\mu m)$	d_{ij} coeff(pm/V)
C-3	2.4	d_{11} = 410
C-4	2.5	d_{11} = 440
C-5	2.3	d_{11} = 630
C-6	2.4	d_{11} = 510
C-7	1.7	d_{12} = 290

Many times, obtaining a value for the d_{ij} coefficient is not enough to determine the usefulness of the material. A good measure of the overall value of the material for nonlinear optical device purposes is the figure of merit (FOM). The second harmonic power is proportional to the square of the dominant element of the **d** tensor. However, the indices of refraction may also be incorporated (see chapter 2) into the expression. Therefore, for second harmonic generation, the FOM is given by equation 4.12.[25]

$$FOM = \frac{d_{eff}^2}{n_\omega^2 n_{2\omega}} \tag{4.12}$$

d_{eff} is the effective d coefficient, and n_ω and $n_{2\omega}$ are the indices of refraction at the fundamental and second harmonic, respectively. The effective d coefficient takes into account the angular dependencies and phase–matchable characteristics of the nonlinear coefficient. For DAST, the d_{11} coefficient is not phase–matchable, however the d_{12} coefficient is. A vague estimate for the figure of merit can be calculated based on a d_{12} of 200 pm/V, yielding a FOM of approximately 4000 $(pm/V)^2$. This value for the FOM can be compared with some other well–characterized compounds such as dimethylamino acetoamidonitrobenzene (DAN) with a FOM of 420 $(pm/V)^2$ or 3-methyl 4-methoxy nitrostilbene (MMONS) with a FOM of 850 $(pm/V)^2$.[4]

Chapter 5

Conclusions

5.1 Results

The mechanism of nonlinear optics has long been modeled as a dipole process. The organic family of materials offers the potential for accurately engineering molecules for enhanced dipolar response to incident or applied fields. One such series of materials was produced based on the stilbene and stilbazole chromophores using a variety of counterions and substituents. The second and third order nonlinear optical properties of these materials were evaluated using powder tests and Maker Fringe experiments.

The powder tests demonstrated some interesting properties with regards to some of the materials. Over fifty different materials were tested; samples that had more than one phase were prepared in each of the phases and tested. The second harmonic numbers ranged from zero for certain centrosymmetric organics, to over 2500 times urea, for some of the best materials. The third harmonic results ranged from negligibly small to over 200 times DANS (this work focused on large second and third harmonic signals). DAST demonstrated the highest second and third harmonic powder efficiencies albeit in slightly different forms. The DAST sample that had been melted and recrystalized gave a second harmonic powder efficiency of approximately 2600 times Urea. On the other hand, the original powder form of DAST produced second harmonic efficiencies of just under 1000 times Urea. However, the recrystalized DAST did not produce the highest third harmonic powder efficiencies. Instead, the original powder sample produced the largest third harmonic powder efficiencies, at 200 times DANS; whereas the recrystalized DAST produced third harmonic efficiencies of only 55 times DANS. One of the other interesting materials was DASM. In its hydrated form,

DASM produced second harmonic powder efficiencies of about 950 times Urea. On the other hand, DASM was not as promising a third order material, producing an efficiency 40 times DANS.

Other aspects of the various materials came to light during the powder tests. Typically, the second harmonic tests were conducted at reasonable pulse energies. However, third order processes required increased intensities. The higher pulse energies approached the damage thresholds of many of the materials. In some cases, damage was noticeable due to the formation of localized charred areas where decomposition had taken place.

The powder tests provided a good approximation to the second and third order optical susceptibilities of the various materials. However, the specific quantification of the nonlinear optical coefficients required a more rigorous experiment. The **d** and **C** coefficient tensors can be measured using the Maker Fringe experiment. However, due to time constraints and a slow crystal growth process, only two tensor elements of the **d** coefficient tensor of DAST were measured.

The DAST crystals were grown via slow evaporation from methanol. The crystals were approximately 200 to 500 μm thick. Single crystal x-ray orientation revealed that the **ab**, or **xy**, plane was contained within the platelet.[2] The fortuitous placement of the crystallographic axes facilitated the measurements of the d_{11} and d_{12} coefficients through the Maker Fringe measurements.

The Maker Fringe experiments were conducted using a discrete rotation of the crystal in the incident beam. Resolutions of 0.1° per increment were possible. Measurements for the d_{11} coefficient exhibited a coherence length, L_c, of 2.4±0.3 μm; the L_c calculation translated to a d_{11} coefficient of 600±100 pm/V. Measurements for the d_{12} coefficient exhibited a coherence length of 1.7±0.2 μm which produced a d_{12} coefficient of 230±50 pm/V. The d_{11} coefficient was not phase–matchable; therefore the d_{12} coefficient provided a vague estimate of d_{eff}, from which the figure of merit was calculated to be on the order of 4000 $(\text{pm/V})^2$.

5.2 DAST Molecular System

The results showed that specific molecular characteristics can be used to enhance the nonlinear optical effect in certain crystals. A conjugated bond system supporting a freer electron motion can help produce increased second and third order optical susceptibilities.

The stilbene and stilbazole family of chromophores offers a single–double alternating bond structure that produced greatly increased optical nonlinearities. Furthermore, substituting proper groups and counterions into the system can result in a larger dipole moment and consequently more observable effects. The use of a dimethyl substitution and the tosylate counterion provided such a properly substituted system in DAST. Furthermore, noncentrosymmetric crystallization translates the molecular nonlinearity to the bulk level. In DAST, the hydrated form of the material crystallizes in space group Cc, point group m. The aspects of the molecular characteristics and crystal packing arrangements were combined in DAST to produce a substance with greatly enhanced second and third order optical susceptibilities.

However, DAST was by no means a perfect molecular system. The nonlinear optical measurements had to be conducted at a fundamental wavelength of 1.907 μm, producing a second harmonic at 953.5 nm. The infra–red wavelength was chosen because DAST has an extremely large absorption band at 650 nm. Thus, any significantly smaller wavelength would have generated irrelevant numbers due to absorption of the second harmonic signal. Unfortunately, the large absorption in the visible spectrum causes more significant problems than those associated with taking measurements at infra–red wavelengths. Systems that may utilize nonlinear optical devices will typically involve semiconductor lasers. The wavelengths may be anywhere from 800 nm to 1.5 μm. A DAST–based device would absorb a substantial portion of any second harmonic radiation. Therefore, continued research on molecular systems is needed to produce a material with not only a high **d** coefficient but also a high degree of transparency.

5.3 Applications

Devices utilizing nonlinear optical effects are typically constructed from inorganic materials such as $LiNbO_3$, KDP, or KTP. However, the coefficients of these substances are moderate and restrict their use to high–power systems, utilizing either high–intensity lasers or high–voltage power supplies, to get observable effects. Therefore, materials with increased nonlinear optical coefficients may make low–power systems more amenable to nonlinear optical devices.

However, even the molecular systems evaluated in this work provide only a one to two

order of magnitude increase over current inorganic systems. Such an increase of 10 to 100 over existing systems is not enough to offset the 10 W to 10 kW requirements, and bring nonlinear optics to low–power systems. Therefore, additional research is required. This research should extend to other methods of reducing the power requirements independent of, but in addition to, enhanced molecular systems design. One promising technology that may be used is waveguiding.

Waveguides have been used in many systems to significantly reduce power requirements, by increasing power densities. In many cases, the increased densities bring power requirements down to the 100 mW to 100 W level.[25] The application, then, of organic molecular system technology to waveguides can reduce these requirements further. A one to two order of magnitude improvement would reduce the power requirements on nonlinear phenomena down to the 1 to 100 mW level, finally allowing nonlinear materials to be used with semiconductor lasers.

5.4 Future Measurements

One of the most interesting and possibly promising results of the work demonstrated here was the generation of theoretical Maker Fringe curves based on the equations derived in chapter 2. From these curves a coherence length and d_{ij} coefficient could be extrapolated. A theoretical curve could be fit to a set of experimental data by slightly changing one of four variables: n_ω, $n_{2\omega}$, the crystal thickness (L), or the coherence length (L_c). By altering the four parameters of the material for a sample curve and for a reference curve, the coherence lengths and peak powers could be extrapolated to give a d_{ij} coefficient.

The process of fitting to experimental data has potential uses in other areas, one of which is thin film nonlinear optics. In many cases, nonlinear optical materials have been placed as thin films on glass or polymer substrates. The Maker Fringe technique was not a completely accurate method for characterizing thin film materials because the thinness of the sample resulted in a curve with no minima (i.e. a single peak or valley). Therefore, a coherence length could not be calculated from the measured data. Instead, the value for $L_c(0)$ was typically calculated from the indices of refraction, which were measured using a Brewster's angle measurement. However, using a theoretical curve fit to the data, the coherence length can be computed from the measurements providing a more accurate value, which can then

be used in the expressions for the d_{ij} and C_{ij} coefficients. Thin film substrates of highly nonlinear materials could be fit to a theoretical expression, measured relative to a thin reference sample, and characterized far more accurately than currently possible.

The potential exists for engineering molecular systems that may have good nonlinear qualities. By using the benefits and advantages of organic systems, enhanced nonlinear optical materials may become available. These materials could be used in bulk form or as thin films when embedded in polymers. In any case, the need will arise to accurately characterize the nonlinear coefficients of the media. This can now be accomplished using the Maker Fringe technique.

Appendix A

The Raman Effect

Raman scattering is the result of a frequency shift of an incoming wave due to an interaction with an active molecule. Quantizing the molecule into various energy states allows a more complete physical description of the process as shown in figure A-1, where *r1* and *r2* represent virtual levels; no real transitions are taking place. The energy separation of any two levels of the molecule can be related to a frequency as in A.1, for the energy between states v and $v+1$.

$$\mathcal{E}_{v,v+1} = \hbar\omega_{v,v+1} \tag{A.1}$$

In the Raman process the two levels involved in the transition typically represent vibrational states of the molecule. To obtain radiation the molecule seems to make a transition of much greater energy than the separation of the vibrational states, to a virtual state followed by an immediate decay to the final state. Ultimately, the transition is between two adjacent vibrational levels. However, by using the virtual states, optical frequencies can be radiated. In reality, there is no real absorption or emission. Instead, a small amount of

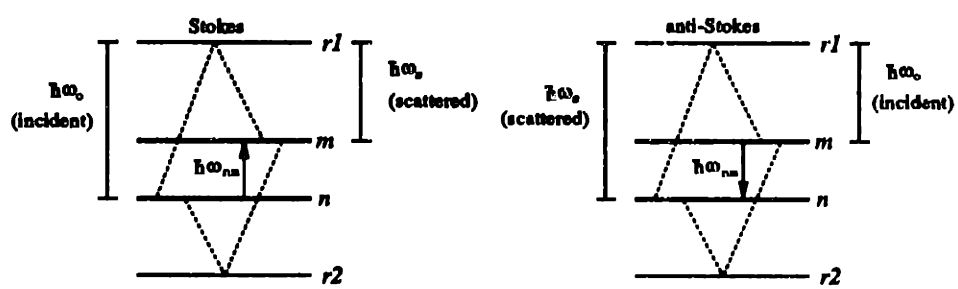

Figure A-1: Raman shift state diagram

energy is removed from (or added to) the incident wave and transferred to (or from) the molecule via the scattering process.

Two scattering events are present in a Raman shift, as indicated in equation A.2, where ω_o is the frequency of the incident wave and ω_v is the amount by which it is shifted.

$$\omega_s = \omega_o \pm \omega_v \tag{A.2}$$

The first process is a downshift in frequency which implies that the molecule was in an unexcited state and absorbed energy making the transition to an excited state. The energy absorbed was removed from the incident wave in the process, known as a Stokes process. The second event involves the opposite; energy is transferred from the molecule to the wave. This process occurs for molecules initially in an excited state transitioning to an unexcited or ground state. This is considered an anti–Stokes process. Because the anti–Stokes process depends on an initial excited state population, the Boltzman distribution indicates that the population is reduced by a factor of $e^{-\frac{\hbar\omega_v}{kT}}$ relative to the unexcited state; and consequently the intensity is reduced by the same amount relative to the Stokes process. Stokes intensity dominates and thus is the process considered here.

A.1 The Scattering Cross–Section

To properly derive the cross section, a semi–classical treatment of the molecular system will be used. Raman scattering lends itself well to the dipole approximation. That is, the molecule in the presence of an applied field can be considered a driven electric dipole, where the electron cloud oscillates around the larger, heavier nuclei. Application of the dipole approximation results in the Hamiltonian as given in A.3.

$$H = H_o - \mu \cdot \mathbf{E} \tag{A.3}$$

In this expression H_o is the Hamiltonian of a molecule in the absence of an applied field; $\mu \cdot \mathbf{E}$ represents the perturbation Hamiltonian due to the electric field and molecular interaction; μ is the electric dipole moment, and $\mathbf{E}$ is the incident electric field. Typically, the interaction term is small compared to the unperturbed Hamiltonian of the molecule and time–dependent perturbation theory can be applied. The wave function of the molecule can

be calculated, and an expectation value for the electric dipole moment derived as given in equation A.4, for a transition from molecular state n to state m, where j and k denote Cartesian components.[20]

$$\langle \mu_j(t) \rangle = \sum_k \left\{ [\alpha_{jk}^{mn}(\omega)]^* E_k^* e^{-i(\omega_o + \omega_{mn})t} + [\alpha_{jk}^{mn}(\omega)] E_k e^{i(\omega_o + \omega_{mn})t} \right\} \tag{A.4}$$

The term α is the transition polarizability associated with this particular transition and is given in equation A.5, where the summation over r covers all intermediate states.

$$\alpha_{mn} = \frac{1}{\hbar} \sum_r \left[\frac{\langle m|M_j|r\rangle\langle r|M_k|n\rangle}{\omega_{rn} + \omega_o} + \frac{\langle m|M_k|r\rangle\langle r|M_j|n\rangle}{\omega_{rn} - \omega_o} \right] \tag{A.5}$$

The expression for the transitional polarizability can be simplified by assuming a static condition. This assumption neglects any translational and rotational motion; the expression can thus be rewritten to account solely for vibrational transitions as given in A.7; the transition is simplified to one between two vibrational states of the molecule, where n indicates quantum numbers for electronic states and v is used for vibrational states.

$$\alpha_{jk}^{vv'} = \frac{1}{\hbar} \sum_{n''} \sum_{v''} \left[\frac{\langle 0v|M_j|n''v''\rangle\langle n''v''|M_k|0v'\rangle}{\omega_{n''v'',0v'} + \omega_o} + \frac{\langle 0v|M_k|n''v''\rangle\langle n''v''|M_j|0v'\rangle}{\omega_{n''v'',0v} - \omega_o} \right] \tag{A.6}$$

Thus, equation A.7, represents the transition polarizability of a transition between a molecular state characterized by v and one by v'. As before, the summation is over all intermediate electronic and vibrational states. The expression may be simplified further by making use of the Born–Oppenheimer approximation. Physically, this approximation implies that the electron clouds follow, without lag, the nuclear vibrational movement of the molecule. This allows the wave function of the molecule (electrons and nuclei) to be written as in A.7, where x and X denote the normal electronic and nuclear coordinates, respectively; χ_{ev_e} is the wave function for the nuclei and ϕ_e is the wave function for the electrons.[9]

$$\psi_m = \chi_{ev_e}(X)\phi_e(x, X) \tag{A.7}$$

The expression in A.7 implies that the electronic and nuclear vibrational states can be separated; in addition the closure property of the nuclear vibrational wave function may also be used to simplify the transitional polarizability and arrive at the expression in A.9.

$$\sum_{v} \chi_{nv}(X')\chi^{*}_{nv}(X) = \delta(X - X') \tag{A.8}$$

$$\alpha^{vv'}_{mn} = \langle v|\alpha_{jk}(\omega, X)|v'\rangle \tag{A.9}$$

where

$$\alpha_{jk}(\omega, X) = \frac{1}{\hbar}\sum_{n''}\left[\frac{\langle 0|M_j|n''\rangle\langle n''|M_k|0\rangle}{\omega_{n''0} + \omega_o} + \frac{\langle 0|M_k|n''\rangle\langle n''|M_j|0\rangle}{\omega_{n''0} - \omega_o}\right] \tag{A.10}$$

$\alpha(\omega, X)$ can be further expanded in a Taylor series with respect to the normal coordinate of nuclear vibration to get A.11, where the X^o is the equilibrium position of the nuclei; only the linear terms in X have been kept (higher order terms relate to multi-photon processes which will not be dealt with here).

$$\alpha(\omega, X) = \alpha(\omega, X^o) + \left(\frac{\partial\alpha}{\partial X}\right)_o X \tag{A.11}$$

The first term, $\alpha(\omega, X^o)$ is independent of the normal coordinate, X, and thus does not cause transitions between adjacent vibrational levels. This term is responsible for scattering events such as Rayleigh scattering and fluorescence. Therefore, keeping only the terms that are associated with transitions, the polarizability can be written as A.12.

$$\langle v|\alpha(\omega X)|v'\rangle = \left(\frac{\partial\alpha}{\partial X}\right)_o \langle v|X|v'\rangle \tag{A.12}$$

The expression of the off-diagonal matrix element of normal mode coordinate between the ground state and the first excited state is given in A.13, where ω_v is the frequency associated with the transition $v \rightarrow v'$. Using A.13, the transition polarizability may be rewritten as given in A.14.[26]

$$\langle v|q|v'\rangle = \sqrt{\frac{v'\hbar}{2\omega_v}} \tag{A.13}$$

$$\alpha_{jk}^{vv'}(\omega) = \left(\frac{\partial \alpha}{\partial X}\right)_o \sqrt{\frac{v'\hbar}{2\omega_v}} \tag{A.14}$$

The rigid quantum mechanical derivation of the transition polarizability yields a useful answer. However, this method provides little or no physical insight into the process. Therefore, a more physically meaningful view may shed additional light on the topic.

For an atomic or molecular system the potential energy may be given as a function of the normal coordinate, X, as shown in A.15.[32].

$$V(X) = aX^2 + bX^3 + \cdots \tag{A.15}$$

This expression appears similar to the equation of a harmonic oscillator, and, in fact, the harmonic oscillator corresponds to the simplest potential energy function for a molecular system. The solutions for such a simple case correspond to a series of equally spaced vibrational levels with energies, $\mathcal{E}_v = \hbar\omega_v(v + \frac{1}{2})$. The induced dipole moment for the molecule is given in equation A.16.

$$\mu = \epsilon_o \alpha E \tag{A.16}$$

As before, α, is the molecular polarizability. In a vibrating molecule the molecular polarizability will be a function of the normal coordinate, X. Neglecting the tensor nature of α, a Taylor series expansion yields the expression in A.17.

$$\alpha(X) = \alpha_o + \left(\frac{\partial \alpha}{\partial X}\right)_o X \tag{A.17}$$

The total induced dipole may now be written in terms of the expanded polarizability, as given in A.18.

$$\mu(X) = \epsilon_o \alpha_o E + \epsilon_o \left(\frac{\partial \alpha}{\partial X}\right)_o XE \tag{A.18}$$

Therefore, the same result arises from some approximations about the behavior and energy of the system or from a rigid quantum mechanical approach. The next step is to apply the dipole moment to a classically radiating dipole to obtain the scattered fields and ultimately the scattering cross-section. The dipole moment can be used to calculate the fields that result from the oscillations. The field produced by the dipole will be the scattered

wave at the shifted frequency. Using the classical expression for a radiating dipole (in the far field, $\mathbf{k} \cdot \mathbf{r} \gg 1$), the equation for the scattered electric field may be given as in A.19, where k_s is the wave vector for the scattered field ($k_s = \frac{\omega_s}{c}$, for $\omega_s = \omega_o - \omega_v$), and η_o is the wave impedance ($\eta_o = \sqrt{\frac{\mu_o}{\epsilon_o}}$).

$$|\underline{\mathbf{E}_s}| = \frac{j\eta_o k_s (j\omega\mu)}{4\pi r} e^{-jk_s r} \sin\theta \tag{A.19}$$

Equation A.16 can then be substituted into the field expression to get A.20, where c is the speed of light in vacuum.

$$|\underline{\mathbf{E}_s}| = \frac{-\eta_o \omega_s^2 \epsilon_o \alpha E_i}{4\pi r c} e^{-jk_s r} \sin\theta \tag{A.20}$$

An expression for the power flux density may now be derived by applying the complex Poynting theorem to the fields. This expression is given in A.21.

$$\langle S_s \rangle = \frac{1}{2} \Re \{E \times H^*\} = \frac{|E|^2}{2\eta} = \frac{\eta_o \omega_s^4 \epsilon_o^2 \alpha^2 E_i^2}{32\pi^2 c^c r^2} \sin\theta \tag{A.21}$$

To arrive at the total scattered power, expression A.21 must be integrated over a sphere. The total scattered power is given in A.22.

$$P_s = \int_0^{2\pi} r d\theta \int_0^{\pi} r \sin\theta d\phi \langle S_s \rangle = \frac{\eta_o \epsilon_o^2 \omega_s^4 v' \hbar}{12\pi c^2 \omega_v} \left(\frac{\partial \alpha}{\partial X} \right)_o^2 E_i^2 \tag{A.22}$$

The incident field is assumed to be a plane wave and thus the corresponding incident power flux density may be given by A.23.

$$\langle S_i \rangle = \frac{E_i^2}{2\eta_o} \tag{A.23}$$

Finally, the scattering cross-section is defined, as before, as scattered power normalized to power flux density. This expression is represented by equation A.24. Substituting the expressions for scattered power and incident power flux density, a scattering cross-section for the Raman effect may be derived; this expression is given in A.25, where S_i is the incident power flux density.

$$Q_s = \frac{P_s}{S_i} \tag{A.24}$$

$$Q_{rs} = \frac{\omega_s^4 v' \hbar}{6\pi c^4 \omega_v} \left(\frac{\partial \alpha}{\partial X}\right)_o^2 \tag{A.25}$$

Raman scattering cross-sections are on the order of 10^{-31} cm^2. For example, the cross-section of H_2 is 1.03×10^{-30} cm^2; in CS_2 it is 6.8×10^{-30} cm^2; and finally in methane, CH_4, it is 2.6×10^{-30} cm^2. These measurements are at an incident wavelength of 488 nm.[32]

A.2 Spontaneous Scattered Intensity

From the previous section, equation A.22 gives an expression for the total scattered power per molecule, at the shifted frequency. Thus, in order to get the total scattered power, the number of molecules, N, must be taken into account. Typically, each transition between different levels yields the same Raman shifted frequency (i.e. the vibrational levels are evenly spaced). However, from equation A.22, the scattered power is dependent upon a factor of v'; for adjacent levels this factor becomes $(v+1)$. Thus, to obtain an expression for the total power radiated, the population of the respective levels must also be taken into account. For a cylindrical chamber of length d (m), and cross-sectional area A (m^2), the volume, V may be given as $V = dA$ (m^3). Given that the chamber is contains a single type of molecule at a particle density of ρ (m^{-3}), the total number of molecules is $N = \rho V$. The fraction of the total population with vibrational quantum number v may be given by the Boltzman distribution law as shown in A.26.

$$f_v = \frac{e^{-\frac{(v+\frac{1}{2})\hbar\omega_v}{kT}}}{\sum_v e^{-\frac{(v+\frac{1}{2})\hbar\omega_v}{kT}}} \tag{A.26}$$

The total scattered power may then be given by the expression in A.27, where all vibrational states are included.

$$P_s = N \sum_v f_v (v+1) \frac{\eta_o \epsilon_o^2 \omega_s^4 v' \hbar}{12\pi c^2 \omega_v} \left(\frac{\partial \alpha}{\partial X}\right)_o^2 E_i^2 \tag{A.27}$$

The summation of the distribution function over all possible vibrational levels may be carried out to yield the expression in A.28.

$$\sum_v f_v (v+1) = \frac{1}{1 - e^{-\frac{\hbar\omega_v}{kT}}} \tag{A.28}$$

The simplification of the Boltzman summation can then be substituted into the expression for the total scattered power to obtain A.29, the total observable scattered power.

$$P_s = \left(\frac{N}{1-e^{-\frac{\hbar\omega_v}{kT}}}\right)\frac{\eta_o\epsilon_o^3\omega_s^4 v'\hbar}{12\pi c^2\omega_v}\left(\frac{\partial\alpha}{\partial X}\right)_o^2 E_i^2 \tag{A.29}$$

However, this expression yields only the power scattered by spontaneous Raman scattering. To perform efficient frequency conversion to the Stokes or anti-Stokes line a stimulated process is required, of which the spontaneous scattering will be a part.

A.3 Stimulated Scattering

The derivation of conversion efficiencies for the spontaneous Raman scattering process was carried out using a semiclassical approach. Unfortunately, the stimulated gain derivation requires a more rigid fully quantum mechanical method. For the theory of spontaneous Raman scattering the interaction was between the normal coordinate of the molecular vibration and the electromagnetic field. For stimulated scattering, the same quantities interact. The Hamiltonian may be given as in equation A.30, where the vibrational energy, the incident wave, and the interaction have been accounted for.

$$H = H_v + H_r + H_{int} \tag{A.30}$$

The individual Hamiltonians are given in A.31, A.32, and A.33, where the s subscript indicates the electric field and frequency associated with the scattered radiation, the L subscript is associated with the incident field, and v indicates the frequency associated with the vibrational state transition. $\mathbf{R}_i$ represents the center of mass coordinate for the i^{th} molecule and the summation is over all molecules. [20][9]

$$H_v = \sum_i \frac{1}{2}\left[\mathbf{p}^2(\mathbf{R}_i) + \omega_v^2\mathbf{q}^2(\mathbf{R}_i)\right] \tag{A.31}$$

$$H_r = \frac{1}{2}\int\left(\epsilon_o\mathbf{E}^2 + \frac{1}{\mu_o}\mathbf{B}^2\right)dV \tag{A.32}$$

$$H_{int} = \sum_i \left(\frac{\partial\alpha}{\partial q}\right)_o \mathbf{q}^2(\mathbf{R}_i)\times[\mathbf{E}_s(\mathbf{R}_i)\cdot\mathbf{E}_L(\mathbf{R}_i)] \tag{A.33}$$

The individual Hamiltonian expressions are given in terms of the momentum, position,

and field operators. The transformations assocaiated with the quantization of the radiation field are given in A.34, A.35, and A.36 for momentum, position, and electric field, respectively.

$$\mathbf{p}(\mathbf{R}_l) = N_o^{-\frac{1}{2}} \sum_k i \left(\frac{\hbar\omega_v}{2}\right)^{\frac{1}{2}} (\hat{a}_k^\dagger - \hat{a}_k) e^{i\mathbf{k}\cdot\mathbf{R}_l} \tag{A.34}$$

$$\mathbf{q}(\mathbf{R}_l) = N_o^{-\frac{1}{2}} \sum_k \left(\frac{\hbar}{2\omega_v}\right)^{\frac{1}{2}} (\hat{a}_k + \hat{a}_k^\dagger) e^{i\mathbf{k}\cdot\mathbf{R}_l} \tag{A.35}$$

$$\mathbf{E}(\mathbf{R}_l) = \sum_k i\hat{\varepsilon} \left(\frac{\hbar\omega}{2\epsilon_o V}\right)^{\frac{1}{2}} (\hat{a}_k^\dagger e^{i\omega_k t - i\mathbf{k}\cdot\mathbf{R}_l} + \hat{a}_k e^{-i\omega_k t + i\mathbf{k}\cdot\mathbf{R}_l}) \tag{A.36}$$

The Hamiltonian may then be written in second quantized form as given in A.37, A.38, A.39. To arrive at these expressions, the identity, $\left(\frac{1}{N_o}\right) \sum e^{i\mathbf{k}\cdot\mathbf{R}_l} = \delta_{k,0}$ has been used along with a series of assumptions. First, the Hamiltonian has been restricted to include only the first Stokes line of the vibrational band since stimulated Raman scattering is a competitive process. Second, the zero–point energy has been neglected and the incident field is assumed to be single mode. Finally, Raman scattering is a process whereby an incident field photon is destroyed, creating a Stokes field photon and a vibrational photon; the reverse is a viable process as well in which an incident field photon is created, destroying a Stokes photon and a vibrational photon, any other transitions are not of interest in this scattering process.

$$H_v = \sum_{k,v} \hbar\omega_v \hat{a}_k^\dagger \hat{a}_k \tag{A.37}$$

$$H_r = \sum_{k,\lambda} \hbar\omega_{k,\lambda} \hat{a}_{k,\lambda}^\dagger \hat{a}_{k,\lambda} \tag{A.38}$$

$$H_{int} = \left(\frac{\partial\alpha}{\partial q}\right)_o \frac{N_o^{\frac{1}{2}} \hbar^{\frac{1}{2}}}{4n^2 V} \sum_{k,s} \left(\frac{2\omega_L \omega_s}{\omega_v}\right)^{\frac{1}{2}} (\hat{\varepsilon}_L \cdot \hat{\varepsilon}_s)(\hat{a}_{k,v}^\dagger \hat{a}_{k,s}^\dagger \hat{a}_{k,L} - \hat{a}_{k,v} \hat{a}_{k,s} \hat{a}_{k,L}^\dagger) \tag{A.39}$$

The transition rate for stimulated Raman scattering can be calculated from Fermi's golden rule given in A.40.

$$W = \frac{1}{\tau} = \frac{2\pi}{\hbar} \sum_f |\langle f|H_{int}|u\rangle|^2 \, \delta(\omega_u - \omega_f) \tag{A.40}$$

For an initial state of $n_{k,v}$, $n_{k,s}$, and $n_{k,L}$ photons in the vibrational, Stokes, and incident

modes, respectively, the only two nonvanishing final states are for the two previously stated conditions. Therefore, the transition rate is given in A.41, where $N = \frac{N_o}{V}$ has been used. In addition, there are assumed to be many more photons in the incident field than in either the Stokes field or vibrational mode, and $n_{k,s}, n_{k,v} \ll n_{k,L}$ has been used.

$$W = N\left(\frac{\partial\alpha}{\partial q}\right)_o^2 \sum_{k,s}\left(\frac{\omega_s\hbar(\hat{\varepsilon}_L\cdot\hat{\varepsilon}_s)^2}{16\omega_v n^2}\right)(1+n_{k,s}+n_{k,v})\frac{4\pi\hbar\omega_L}{n^2V}n_{k,L}\frac{1}{\hbar}\delta(\omega_u-\omega_f) \qquad (A.41)$$

The amplitude of the incident field may be related to the number of photons by the expression in A.42.[9]

$$|\mathbf{E}_L|^2 = \left(\frac{\hbar\omega_L}{n^2V}\right)n_{k,L} \qquad (A.42)$$

Each transition either produces or destroys a Stokes photon. Therefore, the rate of change of Stokes photons is the rate given by Fermi's golden rule, given in A.43, where $n_{k,v}$ has been neglected relative to $n_{k,s}$ as vibrational quanta decay much faster than Stokes photons.

$$\dot{n}_s = N\left(\frac{\partial\alpha}{\partial q}\right)_o^2 \frac{\hbar}{16n^2}\sum_{k,s}\frac{\omega_s}{\omega_v}(\hat{\varepsilon}_L\cdot\hat{\varepsilon}_s)^2(1+n_{k,s})|\mathbf{E}_L|^2\frac{1}{\hbar}\delta(\omega_u-\omega_f) \qquad (A.43)$$

If the Stokes photons are neglected and the summation is carried out over all Stokes modes, the spontaneous scattering cross-section determined in the previous section can be arrived at. However, for stimulated Raman scattering the summation is unnecessary since only Stokes photons of the same mode are amplified.[20] The rate of change of photons for a stimulated process is given in expression A.44.

$$\dot{n}_s = N\left(\frac{\partial\alpha}{\partial q}\right)_o^2 \frac{\hbar}{16n^2}\frac{\omega_s}{\omega_v}(\hat{\varepsilon}_L\cdot\hat{\varepsilon}_s)^2(1+n_{k,s})|\mathbf{E}_L|^2\frac{1}{\hbar}\delta(\omega_u-\omega_f) \qquad (A.44)$$

The delta function can be rewritten in integral form, inclusive of the damping constant of the coherent vibrational excitation, γ, as given in A.45.

$$\delta(\omega_u-\omega_f) = \frac{\gamma}{\pi[(\omega_s-\omega_{s0})^2+\gamma^2]} \qquad (A.45)$$

The substitution of A.45 results in the steady-state spatial gain factor given in A.46.

$$G_{ss} = N\left(\frac{\partial\alpha}{\partial q}\right)_o^2 \frac{\omega_s}{16cn\omega_v}|\mathbf{E}_L|^2 \frac{\gamma}{\pi[(\omega_s - \omega_{s0})^2 + \gamma^2]} = g_{ss} I_L \tag{A.46}$$

Finally, a steady-state gain coefficient for the Stokes intensity, given in A.47 in $\frac{cm}{MW}$, can be derived using $I_L = cn|\mathbf{E}_L|^2$ as the incident laser intensity.

$$g_{ss} = N\left(\frac{\partial\alpha}{\partial q}\right)_o^2 \frac{\omega_s}{16c^2n^2\omega_v} \frac{\gamma}{\pi[(\omega_s - \omega_{s0})^2 + \gamma^2]} \tag{A.47}$$

The gain coefficient leads to an exponential growth in Stokes intensity. To get efficient conversion, the incident intensity must be above a threshold. This limit is given in A.48.[22]

$$I_t \approx \frac{16}{g_{ss}\ell} \tag{A.48}$$

In the setup used for the Maker fringe tests, a 60 cm path-length cell filled with hydrogen gas was used. The steady-state gain for hydrogen gas, with $N \approx 10^{-20}$ cm^{-3}, is 4.89×10^{-3} cm/MW.[20] The incident beam was focused into the cell. The focal length of the lens was 40 cm with a beam radius at the lens of 0.5 cm and an incident wavelength of 1.064 μm, resulting in a diffraction-limited spot size of 0.02 mm^2 at the focus ($w_o \approx \frac{\lambda f}{R}$ where f is the focal length and R is the beam radius at the lens). The incident power was 43 MW (7 ns pulses at 300 mJ). The front window of the cell was 10 cm past the lens, and thus the spot size at this point was 0.4 cm^2. The cell was 60 cm in length, ℓ = 60 cm, resulting in a threshold power flux of 6 MW/cm^2. The spot size at the window was 0.4 cm ^{2} with an incident power of 43 MW resulting in a power flux of 100 MW/cm^2 at the cell window, over 1.5 times the threshold requirement for efficient conversion.

Appendix B

Powder Test Samples

The powder test materials were prepared by a group of organic chemists at the General Electric Corporate Research and Development Center.[3] The organic substances were designed based on the theoretical specifications for enhanced nonlinear optical properties. The powder samples are broken down into subgroups representative of chromophores with different substituent groups and combinations of different counterions.

Table B.1: Organic reference compounds

Ref. No.	Organic Compound
A1	Urea
A2	MNA
A3	MNMA
A4	Trimons
A5	DANS
A6	4-OH NS
A7	POM

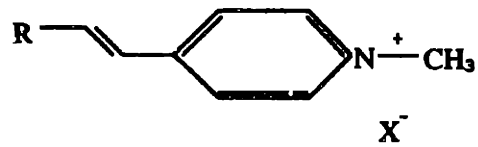

Figure B-1: 1-N–Methyl Stilbazolium chromophore

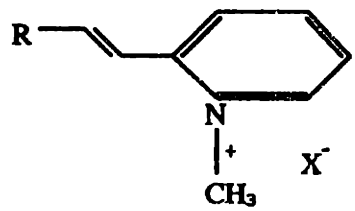

Figure B-2: 3-N–Methyl Stilbazolium chromophore

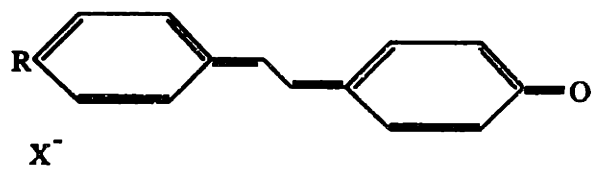

Figure B-3: 1-O Stilbene chromophore

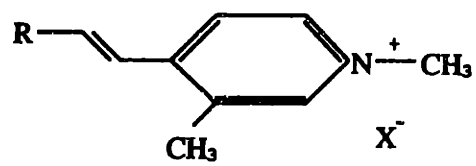

Figure B-4: Modified Stilbazole chromophore

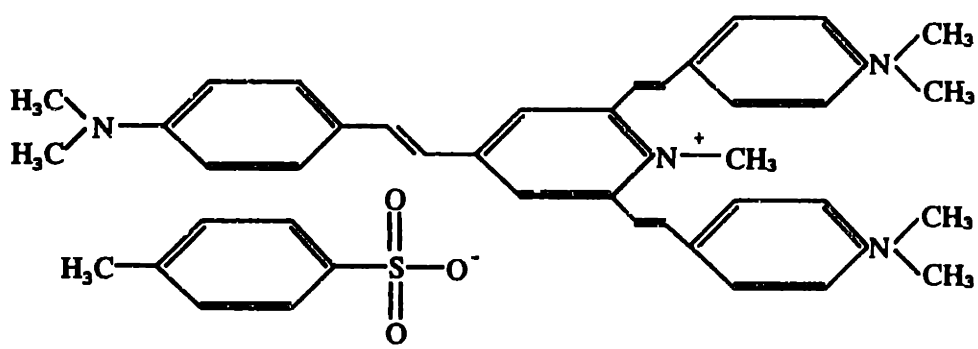

Figure B-5: DAST[3]

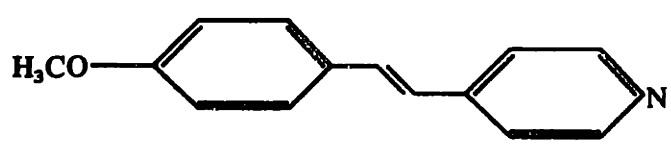

Figure B-6: 4–Methoxy Stilbazolium

Table B.2: 1-N-Methyl Stilbazolium salts

Ref. No.	R(phase)	X^-
B1	4-O=C_6H_4-	
B2	4-$(CH_3)_2NC_6H_4$-(1)	$CH_3SO_3^-$
B3	4-$(CH_3)_2NC_6H_4$-(2)	$CH_3SO_3^-$
B4	4-$(CH_3)_2NC_6H_4$-(3)	$CH_3SO_3^-$
B5	4-$(CH_3)_2NC_6H_4$-(4)	$CH_3SO_3^-$
B6	4-$(CH_3)_2NC_6H_4$-(5)	$CH_3SO_3^-$
B7	4-$(CH_3)_2NC_6H_4$-(6)	$CH_3SO_3^-$
B8	4-$(CH_3)_2NC_6H_4$-(7)	$CH_3SO_3^-$
B9	4-$(CH_3)_2NC_6H_4$-(1)	p-$CH_3C_6H_4SO_3^-$
B10	4-$(CH_3)_2NC_6H_4$-(2)	p-$CH_3C_6H_4SO_3^-$
B11	4-$(CH_3)_2NC_6H_4$-(3)	p-$CH_3C_6H_4SO_3^-$
B12	4-$(CH_3)_2NC_6H_4$-(1)	$C_6H_5SO_3^-$
B13	4-$(CH_3)_2NC_6H_4$-(2)	$C_6H_5SO_3^-$
B14	4-$(CH_3)_2NC_6H_4$-(3)	$C_6H_5SO_3^-$
B15	4-$(CH_3)_2NC_6H_4$-	$CH_3SO_4^-$
B16	4-$(CH_3)_2NC_6H_4$-	$CH_3C_6H_4CO_2^-$
B17	4-$(CH_3)_2NC_6H_4$-	$C_6H_4CO_2^-$
B18	4-$CH_3OC_6H_4$-(1)	p-$CH_3C_6H_4SO_3^-$
B19	4-$CH_3OC_6H_4$-(2)	p-$CH_3C_6H_4SO_3^-$
B20	3,4-$(OH)_2C_6H_3$	p-$CH_3C_6H_4SO_3^-$
B21	4-OHC_6H_4-(1)	p-$CH_3C_6H_4SO_3^-$
B22	4-OHC_6H_4-(2)	p-$CH_3C_6H_4SO_3^-$
B23	4-$(CH_3)_2NC_6H_4$-CH=CH-(1)	p-$CH_3C_6H_4SO_3^-$
B24	4-$(CH_3)_2NC_6H_4$-CH=CH-(2)	p-$CH_3C_6H_4SO_3^-$
B25	4-$(CH_3)_2NC_6H_4$-	I^-
B26	4-$(CH_3)_2NC_6H_4$-	PF_6^-
B27	4-OHC_6H_4-	I^-
B28	4-OHC_6H_4-	Br^-
B29	4-OHC_6H_4-	Cl^-
B30	4-$(CH_3)_2NC_6H_4$-	$Cl_3C_6H_2SO_3^-$
B31	4-FC_6H_4-	p-$CH_3C_6H_4SO_3^-$
B32	4-ClC_6H_4-	p-$CH_3C_6H_4SO_3^-$
B33	4-BrC_6H_4-	p-$CH_3C_6H_4SO_3^-$
B34	4-FC_6H_4-	$C_6H_5SO_3^-$

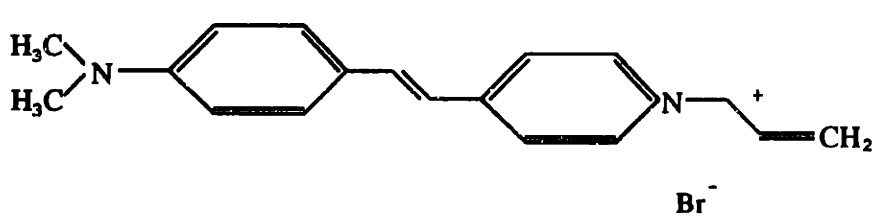

Figure B-7: Modified DimethylAmino Silbazole

Table B.3: 3-N–Methyl Stilbazolium salts

Ref. No.	R(phase)	X^-
C1	4-OHC_6H_4-	p-$CH_3C_6H_4SO_3^-$
C2	4-$(CH_3)_2NC_6H_4$-(1)	I^-
C3	4-$(CH_3)_2NC_6H_4$-(2)	I^-
C4	4-$(CH_3)_2NC_6H_4$-	$C_6H_5SO_3^-$
C5	4-$(CH_3)_2NC_6H_4$-	p-$CH_3C_6H_4SO_3^-$
C6	4-$CH_3OC_6H_4$-	$C_6H_5SO_3^-$
C7	4-$CH_3OC_6H_4$-(1)	I^-
C8	4-$CH_3OC_6H_4$-(2)	I^-
C9	4-$CH_3OC_6H_4$-	p-$CH_3C_6H_4SO_3^-$

Table B.4: 1-O Stilbene salts

Ref. No.	R	X^-
D1	4-$CH_3NC_5H_4$-	I^-
D2	4-$C_{22}H_{45}NC_5H_4$-	

Table B.5: Modified Stilbazole salts

Ref. No.	R	X^-
E1	4-$(CH_3)_2NC_6H_4$-	p-$CH_3C_6H_4SO_3^-$
E2	4-OHC_6H_4-	I^-

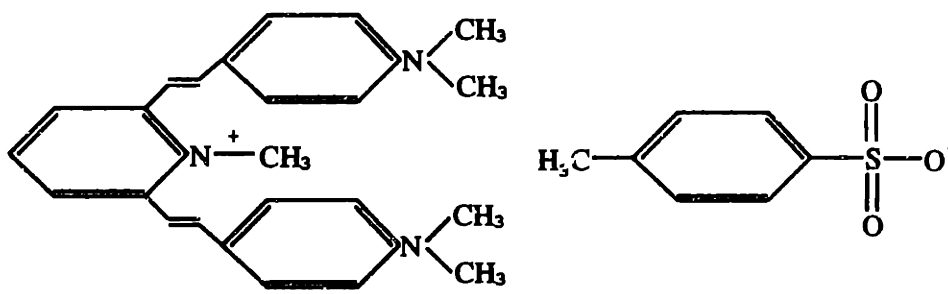

Figure B-8: DAST[2]

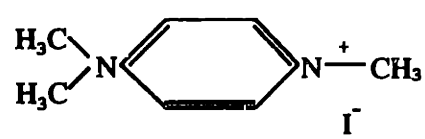

Figure B-9: 4-DimethylAmino 1-N Pyridine

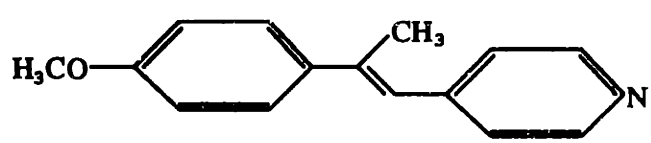

Figure B-10: Modified 4-Methoxy Stilbene

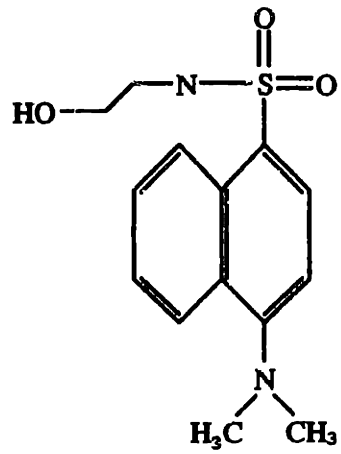

Figure B-11: 2 Pyridine complex

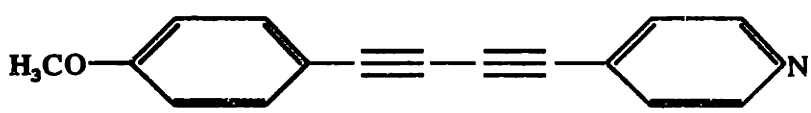

Figure B-12: Substituted triple bond structure

Table B.6: General unclassified salts

Ref. No.	Figure
F1	B-5
F2	B-6
F3	B-7
F4	B-8
F5	B-9
F6	B-10
F7	B-11
F8	B-12

Appendix C

Maker Fringe Measurements

The Maker Fringe experiments were conducted relative to a lithium niobate ($LiNbO_3$) reference crystal 1 mm thick. The indices of refraction, and coherence length for the d_{33} coefficient are given at the specified wavelengths. Experimental data for lithium niobate and the coherence length measurements are given in figures C-1 and C-2.

$$L = 10^{-3}m = 1mm$$

$$n_\omega = 2.1281$$

$$n_{2\omega} = 2.1625$$

$$L_c = \frac{\lambda}{4(n_{2\omega} - n_\omega)} = 13.8 \times 10^{-6}m = 13.8\mu m$$

The only material tested using the Maker Fringe experiment was DimethylAmino Stilbazolium Tosylate (DAST); the various material characteristics are given at the fundamental and second harmonic frequencies. A series of experimental measurements are shown with the calculations done to determine the coherence length, d_{11} or d_{12} coefficients, and the figure of merit (FOM). In the figures, the solid line represents the second harmonic intensity of DAST, and the dotted line represents lithium niobate.

$$L_1 = 1.9 \times 10^{-4} = 190\mu m$$

$$L_2 = 2.05 \times 10^{-4} = 205\mu m$$

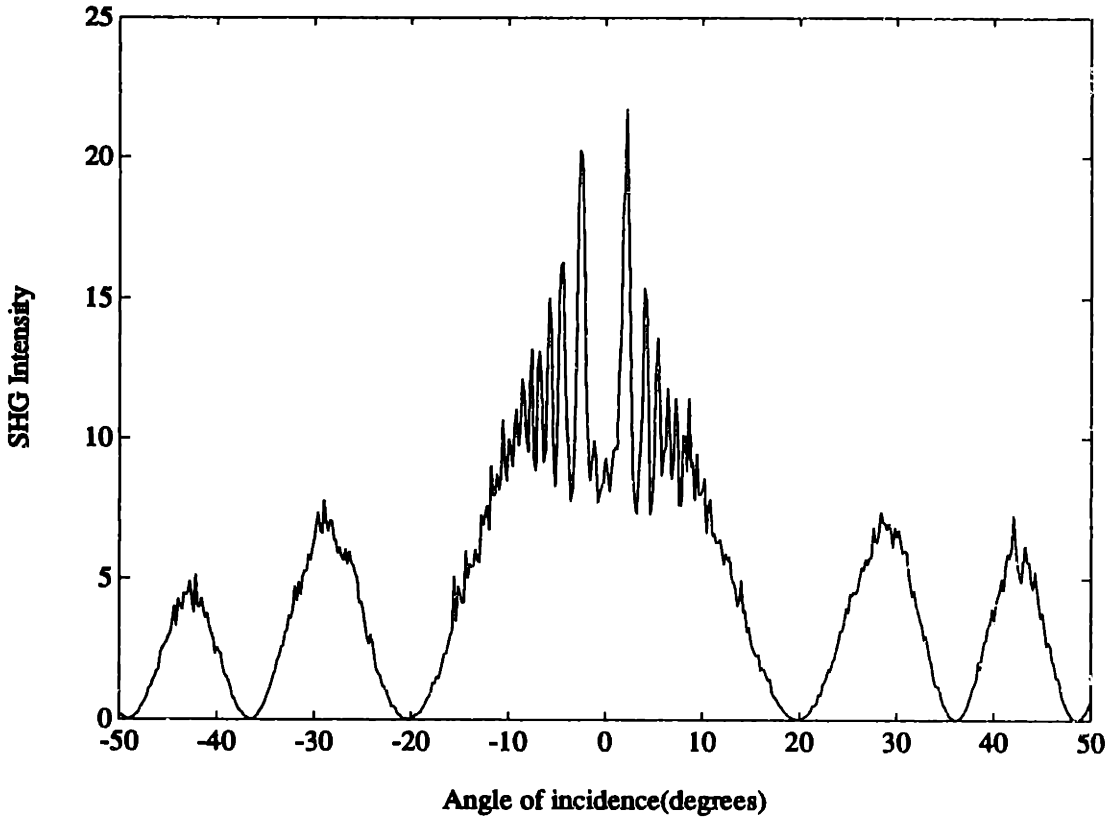

Figure C-1: Experimental Maker Fringe data for Lithium Niobate d_{33}

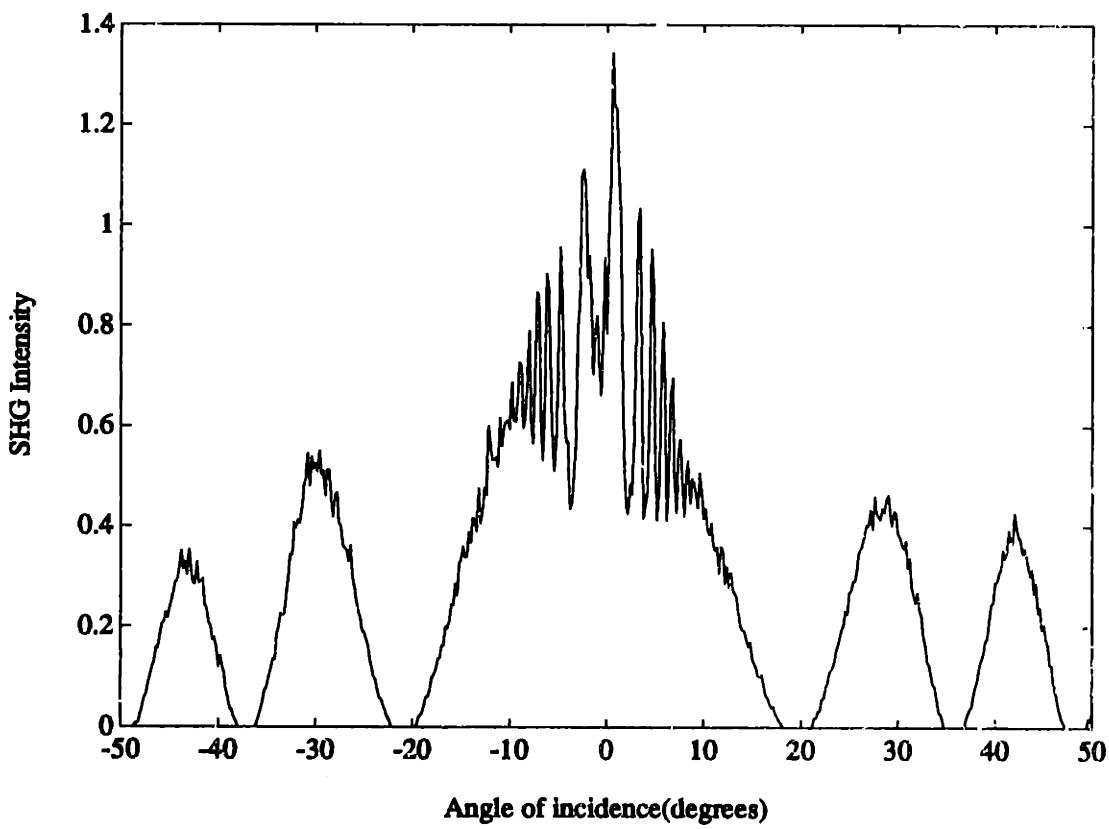

Figure C-2: Experimental Maker Fringe data for Lithium Niobate d_{33}

Table C.1: Lithium Niobate Maker Fringe results

Figure	$L_c(\mu m)$
C-1	13.9
C-2	13.9

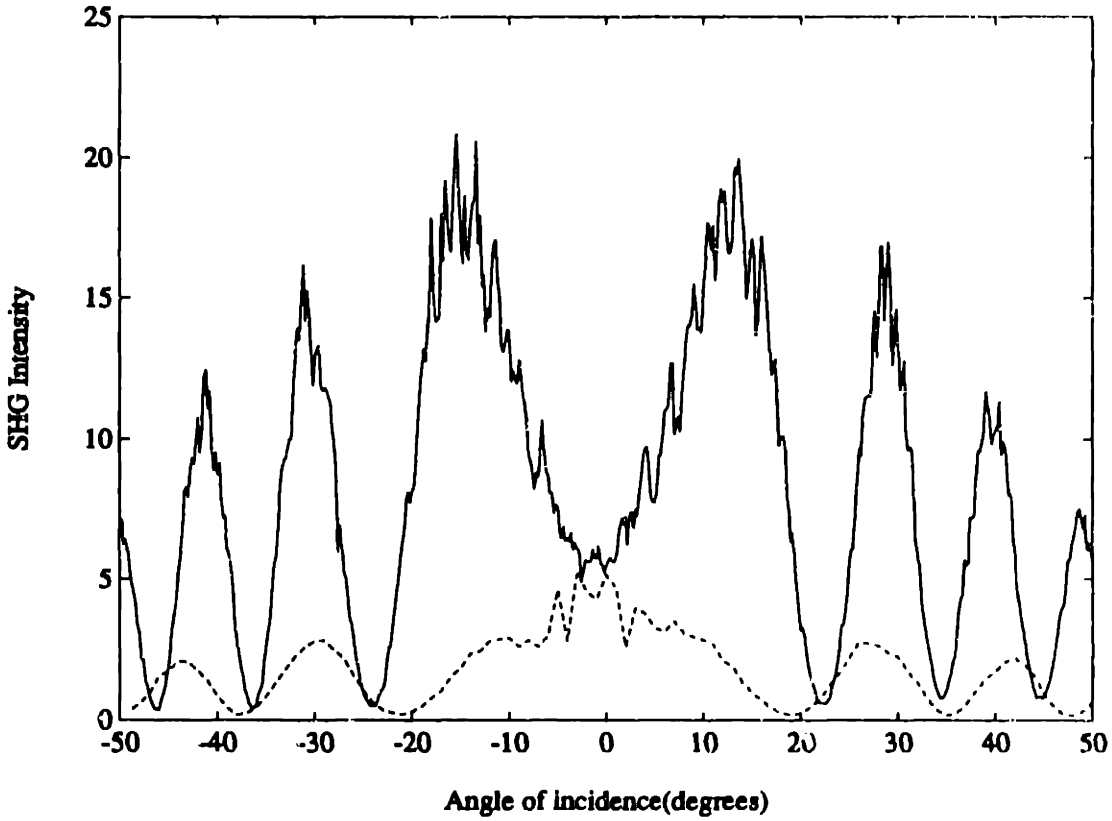

Figure C-3: Experimental Maker Fringe data for DAST d_{11}

$$n_{\omega,x} = 1.988$$

$$n_{\omega,y} = 1.9021$$

$$n_{2\omega} = 2.18$$

$$L_{c,d11} = \frac{\lambda}{4(n_{2\omega} - n_{\omega})} = 2.488 \times 10^{-6} m = 2.488 \mu m$$

$$L_{c,d12} = \frac{\lambda}{4(n_{2\omega} - n_{\omega})} = 1.716 \times 10^{-6} m = 2.716 \mu m$$

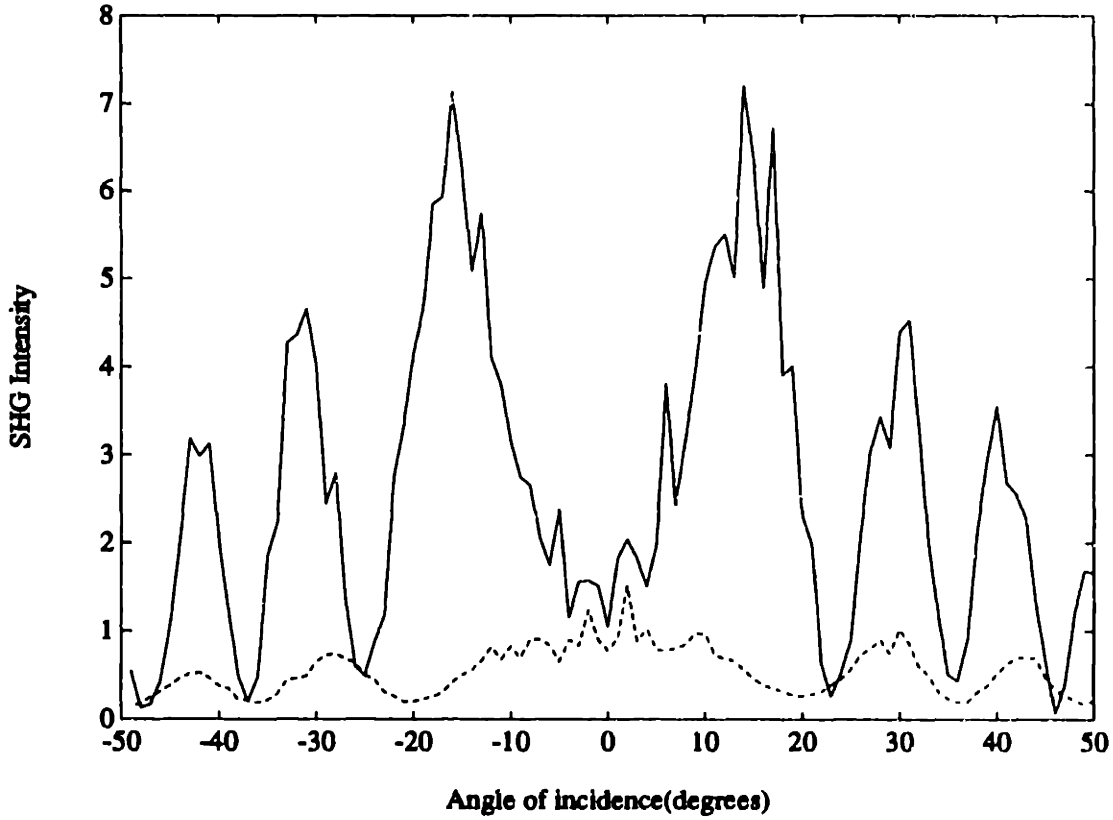

Figure C-4: Experimental Maker Fringe data for DAST d_{11}

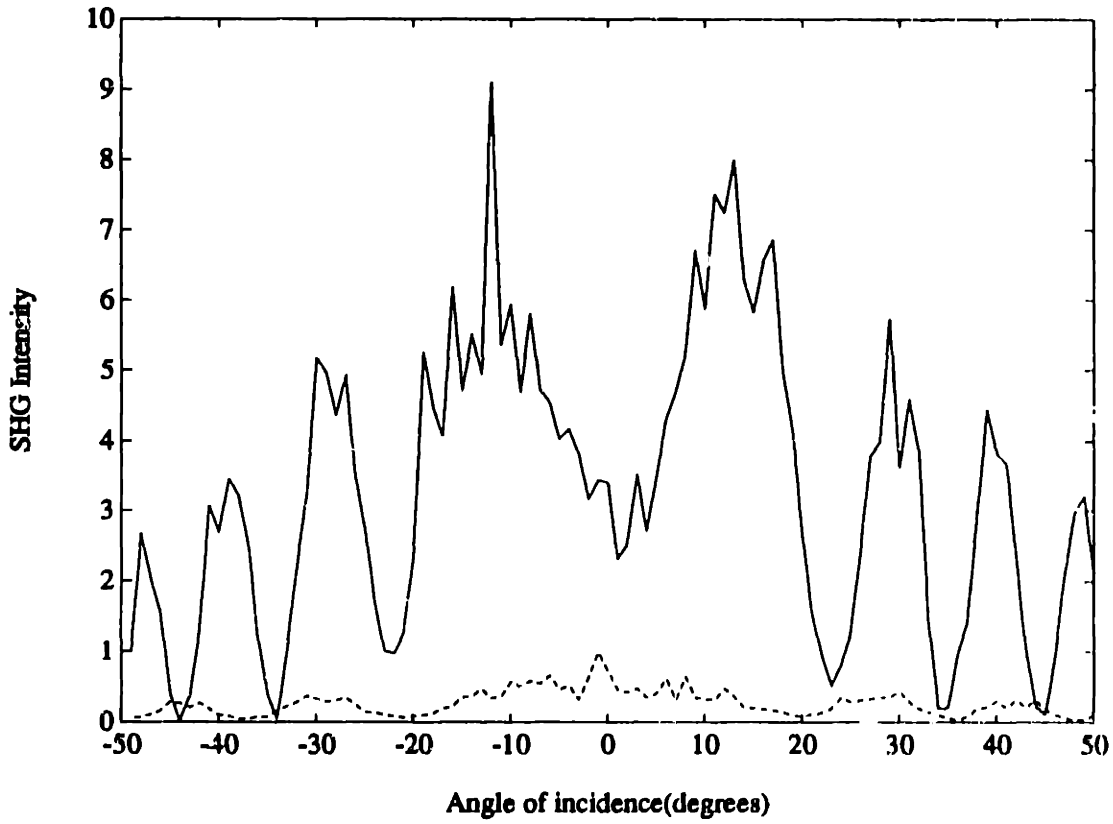

Figure C-5: Experimental Maker Fringe data for DAST d_{11}

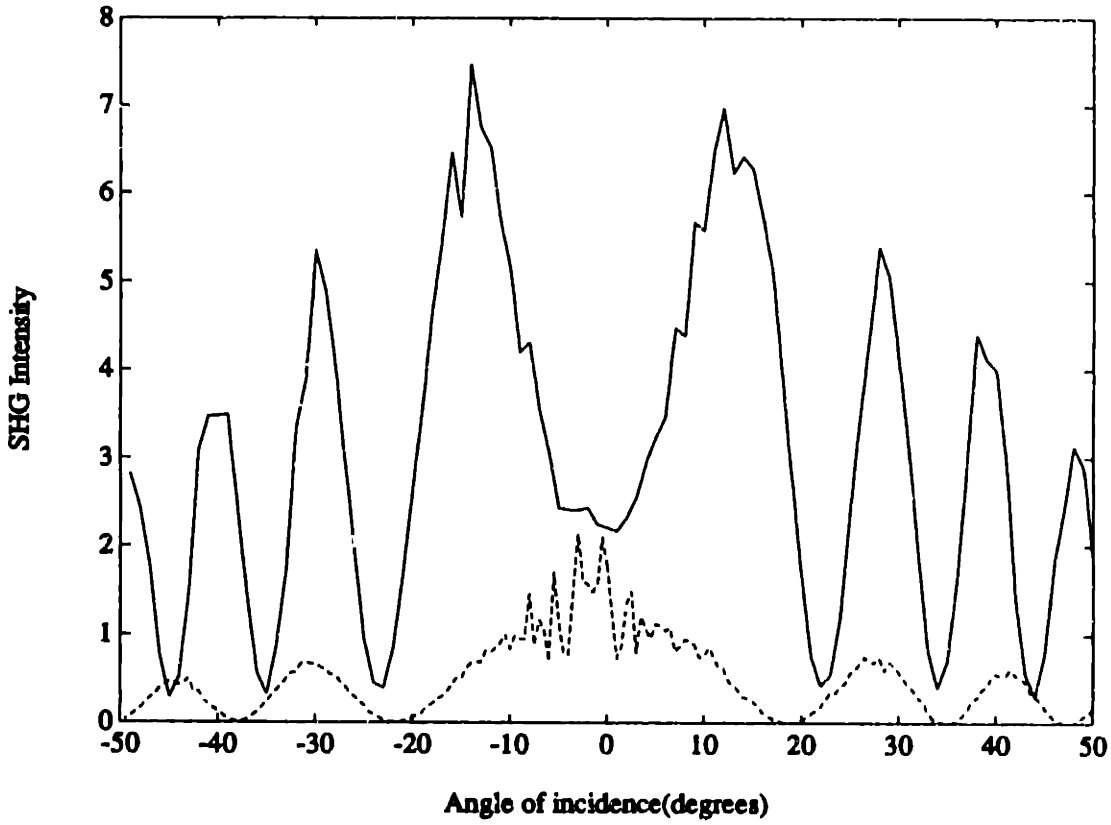

Figure C-6: Experimental Maker Fringe data for DAST d_{11}

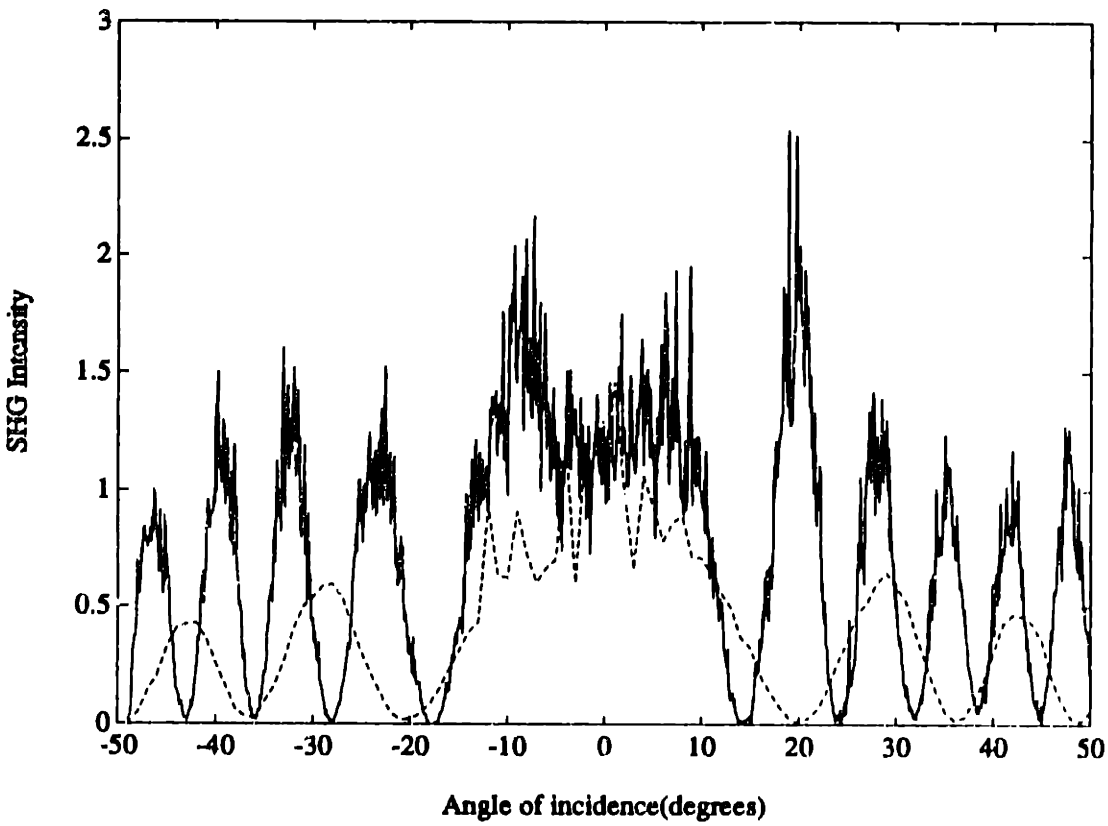

Figure C-7: Experimental Maker Fringe data for DAST d_{12}

Table C.2: DAST Maker Fringe results

Figure	$L_c(\mu m)$	d_{ij} coeff(pm/V)
C-3	2.4	$d_{11} = 410$
C-4	2.5	$d_{11} = 440$
C-5	2.3	$d_{11} = 630$
C-6	2.4	$d_{11} = 510$
C-7	1.7	$d_{12} = 290$

Bibliography

[1] G. C. Baldwin. *Introduction to Nonlinear Optics.* Plenum Press, New York, NY, 1969.

[2] C. P. Yakymyshyn, S. R. Marder, K. R. Stewart, E. P. Boden, J. W. Perry, and W. P. Schaefer. In R. A. Hann and D. Bloor, editors, *Organic Materials for Nonlinear Optics II.* Royal Society of Chemistry, 1991.

[3] Dr. E. P. Boden, P. G. Phelps, Dr. K. R. Stewart, Dr. S. R. Marder (JPL), and Dr. G. Gaines Jr. (RPI). GE CRD, Schenectady, NY 12301.

[4] D. F. Eaton. *Science*, 253:281, 1991.

[5] J. Jerphagnon and S. K. Kurtz. *J. Appl. Phys.*, 41(4):1667–1681, 1970.

[6] D. A. Kleinman. *Phys. Rev.*, 126:1977, 1962.

[7] K. Kubodera. *Nonlinear Optics*, 1:71–80, 1991.

[8] S. K. Kurtz and T. T. Perry. *J. Appl. Phys.*, 39:3798, 1968.

[9] R. Loudon. *The Quantum Theory of Light.* Clarendon Press, Oxford, 2 edition, 1983.

[10] M. J. Weber, D. Milam, and W. L. Smith. *Opt. Engineering*, 17(5):463, 1978.

[11] M. Sheik-bahae, A. A. Said and E. W. Van Stryland. *Optics Letters*, 14(17):955–957, 1989.

[12] M. Sheik-bahae, A. A. Said, et. al. Z-scan: A simple and sensitive technique for nonlinear refraction measurements. In *Nonlinear Optical Properties of Materials.* SPIE, 1989.

[13] G. R. Meredith. In D. J. Williams, editor, *Nonlinear Optical Properties of Organic and Polymeric Materials*, page 30. American Chemical Society, 1983. ACS Symposium Series 233, Washington, DC.

[14] Peter W. Milonni and Joseph H. Eberly. *Lasers*. John Wiley & Sons, New York, NY, 1988.

[15] J. F. Nicoud and R. W. Twieg. In D. S. Chemla and J. S. Zyss, editors, *Nonlinear Optical Properties of Organic Molecules and Crystals*, volume 1 and 2. Academic Press, Orlando, FL, 1987.

[16] J. L. Oudar and D. S. Chemla. *J. Chem. Phys.*, 66:2664, 1977.

[17] P. D. Maker, R. W. Terhune, M. Nisenoff, and C. M. Savage. *Phys. Rev. Letters*, 8(1):21–22, 1962.

[18] R. Lytel, G. F. Lipscomb, and others. In S. R. Marder, J. E. Sohn, and G. D. Stucky, editor, *Materials for Nonlinear Optics: Chemical Perspectives*, page 103. American Chemical Society, 1991. ACS Symposium Series 455.

[19] R. W. Minck, R. W. Terhune, and W. G. Rado. *Appl. Phys. Letters*, 3(10):181, 1963.

[20] H. Rabin and C. L. Tang, editors. *Quantum Electronics: A Treatise*, volume 1 A. Academic Press, New York, NY, 1975.

[21] S. R. Marder, J. W. Perry, and W. P. Schaefer. *Science*, 245:626, 1989.

[22] R. G. Smith. *Applied Optics*, 11:2489, 1972.

[23] G. I. Stegeman. In S. R. Marder, J. E. Sohn, and G. D. Stucky, editor, *Materials for Nonlinear Optics: Chemical Perspectives*, page 113. American Chemical Society, 1991. ACS Symposium Series 455.

[24] B. P. Stoicheff. In P. A. Miles, editor, *Quantum Electronics and Coherent Light*. Italian Physical Society, 1964.

[25] R. H. Stolen and G. I. Stegeman. *Optics News*, pages 8–13, 1989.

[26] H. A. Szymanski, editor. *Raman Spectroscopy Theory and Practice*. Plenum Press, Buffalo, NY, 1967.

[27] M. C. Tobin. *Laser Raman Spectroscopy*, volume 35. John Wiley and Sons, New York, NY, 1971.

[28] V. G. Dmitriev, G. G. Gurzadyan and D. N. Nikogosyan. *Handbook of Nonlinear Optical Crystals.* Springer–Verlag, Berlin, 1991.

[29] W. T. Lotshaw, B. L. Lawrence, and others. Nonlinear optical properties of single crystal organic molecular salts. In *Proceedings of the International Quantum Electronics Conference*, 1992.

[30] M. J. Weber, editor. *Optical Materials*, volume 3 of *Handbook of Laser Science and Technology.* CRC, 1991.

[31] C. P. Yakymyshyn. Private communication.

[32] A. Yariv. *Quantum Electronics.* John Wiley and Sons, New York, NY, 3 edition, 1989.

[33] A. Yariv and P. Yeh. *Optical Waves in Crystals.* John Wiley and Sons, New York, NY, 1984.